Parkin-dependent ubiquitination of TAX1BP1 affects the degradation pathway of defective mitochondria

Anna Lechado-Terradas[1, *], Bianca Lemke[2], Katharina I. Zittlau[2, #], Boris Macek[2], Philipp J. Kahle[1, 3, *]

[1]Laboratory of Functional Neurogenetics, Department of Neurodegeneration, Hertie Institute for Clinical Brain Research and German Center for Neurodegenerative Diseases, Faculty of Medicine, University of Tübingen, Tübingen, Germany.

[2]Quantitative Proteomics Group, Department of Biology, Interfaculty Institute of Cell Biology, University of Tübingen, Tübingen, Germany.

[3]Department of Biochemistry, Faculty of Science, University of Tübingen, Tübingen, Germany.

[#]present address: Laboratory for Structural Mass Spectrometry, Department of Biomolecular Sciences, Weizmann Institute of Science, Rehovot, Israel.

*Corresponding author(s): philipp.kahle@uni-tuebingen.de, anna.lechado-terrads@uni-tuebingen.de

Keywords: Autophagosome, endosome, mitophagy, parkin, TAX1BP1, ubiquitination

Abstract

In stressed cells, the recessive Parkinson disease (PD) associated gene products PINK1 and parkin mediate the autophagic removal of damaged mitochondria (mitophagy). Upon mitochondrial membrane potential disruption, PINK1 phosphorylation activates the ubiquitin ligase parkin which ubiquitinates various mitochondrial protein substrates. These feed-forward modifications on the mitochondria surface attract ubiquitin-binding autophagy receptors that target ubiquitinated mitochondria for degradation. Investigating post-translational protein modifications during this process, we detected transient ubiquitination of K549 within the third coiled-coil domain (CC3) of TAX1BP1 in HeLa cells expressing wild-type (WT) but not catalytically inactive parkin. Parkin-dependent ubiquitination did not target TAX1BP1 to proteasomal degradation but was rather indicative of a regulatory modification. In cells with the full complement of autophagy receptors, TAX1BP1 plays only a minor role in mitophagy. However, when expressed as a sole autophagy receptor, both WT and ubiquitination deficient TAX1BP1 were capable of promoting mitophagy, albeit mitochondria degradation was slightly delayed under mutant conditions. Use of the lysosomal inhibitor bafilomycin A indicated classical autophagolysosomal targeting of damaged mitochondria mediated by WT TAX1BP1. However, for the ubiquitination-deficient TAX1BP1, we observed an increased prevalence of enlarged endolysosomal vesicles carrying accumulated TAX1BP1-positive autophagosomes filled with mitochondrial material. Thus, while ubiquitination of the CC3 domain of TAX1BP1 is not essential for complete mitophagy, the lack of CC3 in TAX1BP1 reroutes the degradation flux to a less efficient endolysosmal degradative pathway. Interestingly, the PD gene product VPS35 becomes prominently engaged in this alternative mitophagy pathway.

Keywords

Autophagosome, endosome, mitophagy, parkin, TAX1BP1, ubiquitination.

Abbreviations

5KO: penta knock-out HeLa; ATG9A: autophagy-related protein 9A; BafA: Bafilomycin A; CALCOCO2/NDP52: calcium binding and coiled-coil domain 2; CC3: third coiled-coil domain of TAX1BP1; CCCP: carbonyl cyanide m-chlorophenylhydrazone; CD63: CD63 antigen; COX4: cytrochrome c oxidase subunit 4; CS: citrate synthase; HSP60: heat shock protein 60; LC3B: microtubule-associated protein 1 light chain 3 beta; MFN1: mitofusin-1; MMF: membrane fraction; MTF: mitochondria fraction; MYO6: unconventional myosin-VI; NBR1: NBR1 autophagy cargo receptor; OMM: outer mitochondrial membrane; OPTN: optineurin; SQSTM1/p62: sequestosome-1; PD: Parkinson disease; PINK1: serine/threonine-protein kinase PINK1; PRKN: E3-ligase parkin; PTM: post-translational modification; RAB7: ras-related protein rab-7a; SSBP1: single-stranded DNA-binding protein; TAX1BP1: Tax1-binding protein 1 homolog; TBC1D15: TBC1 domain family member 15; TOM20: translocase of outer membrane 20 kDa subunit; UBD: ubiquitin binding domain; VDAC: voltage-dependent anion channel; VPS35: Vacuolar protein sorting-associated protein 35; WDR45B: WD repeat domain phosphoinositide-interacting protein 3; WT: wild-type.

65 **Introduction**

66 Mitochondrial quality control and turnover are essential for cellular homeostasis. Cellular
67 stress associated with mitochondrial membrane depolarization induces a pathway leading to
68 removal of damaged mitochondria activated by the two most common recessive Parkinson
69 disease (PD) associated gene products, PINK1 (phosphatase and tensin homolog induced
70 kinase 1) and PRKN (E3 ligase parkin) [1–4]. Under basal conditions, the nuclear encoded
71 PINK1 protein is efficiently imported into mitochondria, where it is rapidly degraded. Upon
72 dissipation of the mitochondrial membrane potential, PINK1 lacks the driving force for
73 mitochondrial import and hence accumulates on the mitochondrial outer membrane (OMM).
74 There, the PINK1 kinase domain faces the cytosol to phosphorylate ubiquitin and the
75 ubiquitin-like domain of parkin, a process which activates the ubiquitin ligase parkin
76 recruited to the OMM of depolarized mitochondria [5–8]. Various ubiquitin linkages target
77 proteins from depolarized mitochondria to proteasomal and autophagic degradation [9]. Five
78 major selective autophagy receptors have been implicated to connect ubiquitinated
79 mitophagy cargo with the autophagy machinery, including SQSTM1/p62 (sequestosome-1),
80 OPTN (optineurin), CALCOCO2/NDP52 (calcium binding and coiled-coil domain 2), NBR1
81 (NBR1 autophagy cargo receptor), and TAX1BP1 (Tax1 binding protein 1) [2,10–12]. These
82 selective autophagy receptors do not statically bridge ubiquitinated mitophagy cargo with
83 membranes containing the lipidated form of LC3B (microtubule-associated protein 1 light
84 chain 3 beta), but can be dynamically regulated by post-translational modifications (PTMs).
85 These PTMs are critical modulators of their function and contribute to the recruitment of
86 autophagy-related proteins involved in autophagosome biogenesis (i.e: ATG9 vesicles or the
87 unc-51 like autophagy activating kinase 1 complex) [13–16]. For example, phosphorylation

88 by TANK binding kinase 1 contributes to important regulatory dynamics of OPTN and
89 NDP52 for selective autophagic removal of damaged mitochondria [10,12,16].

90 Investigating the phospho-proteome and ubiquitylome throughout the time course of
91 mitophagy in catalytically active parkin expressing HeLa cells [17], we detected transient
92 ubiquitination of TAX1BP1 at K549 within the third coiled-coil domain (CC3) of this
93 autophagy receptor. Validation of TAX1BP1 ubiquitination in cells expressing wild-type
94 (WT) or a ligase-dead parkin mutant (C431A), confirmed parkin-dependent ubiquitination
95 of the autophagy receptor at early stages of mitophagy. Removal of the highly ubiquitinated
96 CC3 domain of TAX1BP1 reduced TAX1BP1 distribution on mitochondrial material and
97 induced the engulfment of accumulated autophagosomes into enlarged endolysosomal
98 vesicles (potential amphisomes), apparently rerouting the mitophagy pathway to the
99 endolysosomal system. Thus, the ubiquitinatable CC3 of TAX1BP1 directs depolarized
100 mitochondrial material to autophagosomal degradation, whereas CC3 perturbation mediates
101 the degradation of accumulated autophagosomes with damaged mitochondrial cargo through
102 a less efficient pathway involving endolysosomal trafficking into enlarged endolysosomes.
103 Interestingly, the PD gene product VPS35 (VPS35 retromer complex component) became
104 prominently engaged in the alternative mitophagy pathway described in this study, clearly
105 recognizing the surroundings of the identified enlarged degradative vesicles.

106

107

108

Results

Transient ubiquitination of TAX1BP1 in Parkin-dependent mitophagy

Examining the ubiquitylome of HeLa cells stably expressing parkin treated with the mitochondrial uncoupler carbonyl cyanide m-chlorophenylhydrazone (CCCP) [17], we detected transient ubiquitination of TAX1BP1 at K549 (**Figure 1A and B**). The ubiquitination-indicating di-glycine motifs were detected by mass spectrometry predominantly for TAX1BP1 peptides containing K549, with only minor signals for K571, also located in the CC3 region, and K439, upstream of CC3 (**Figure 1A and B**). TAX1BP1 ubiquitination only occurred in cells expressing WT parkin, but not the catalytically inactive form (C431A-parkin) (**Figure 1B**). Other studies previously reported K549-TAX1BP1 to be increasingly ubiquitinated in a parkin-dependent manner and to follow a similar time course as the one described here [18]. Validation of parkin-dependent ubiquitination of TAX1BP1 via western blotting confirmed the differences between WT- and C431A-parkin observed in the mass-spectrometry screen (**Figure 1C**). In HeLa cells stably expressing active parkin, but not ligase-inactive C431A-parkin, CCCP treatment caused a band shift compatible with TAX1BP1 poly-ubiquitination peaking around 4 h after mitochondrial membrane depolarization. TAX1BP1 ubiquitination vanished at later time points of mitophagy, when parkin substrates like TOM20 (translocase of outer mitochondrial membrane 20) and VDAC (voltage dependent anion channel) were degraded (**Figure 1C**).

To confirm that the observed TAX1BP1 band shifts reflect ubiquitination of the autophagy adaptor, ubiquitin pulldown experiments were performed in the WT-Parkin HeLa cell line

131 (**Figure 1D**). After short CCCP depolarization, some parkin-dependent substrates were
132 pulled down such as ubiquitinated (Ub-) TOM20 as well as ubiquitin in its unmodified form
133 (Total Ub) or the Ser65-phosphorylated version (pS65-Ub) (**Figure 1D**). The appearance of
134 a smear-like band shift for TAX1BP1 was also detected under the same conditions, which
135 contrasted with the absence of a smear observed under basal or bead control pulldown
136 conditions (**Figure 1D**). This data confirms the ubiquitination nature of
137 endogenousTAX1BP1 occurring in a parkin-dependent mitophagy context.

138 Overall, TAX1BP1 levels decreased parallelly to VDAC and TOM20 degradation during
139 early depolarization (2-4 h CCCP) but increased after extended depolarization (8-18 h CCCP)
140 (**Figure 1C**), indicating that early steps of mitophagy might also involve some degradation
141 of the autophagy receptor along with mitochondrial cargo. As early stages of PINK1/parkin
142 mitophagy rely on proteasomal degradation of immediate-early parkin substrates, we
143 checked if the identified ubiquitination of TAX1BP1 could target the autophagy receptor for
144 early proteasomal degradation. In order to test this, HeLa cells stably expressing parkin were
145 transfected with TAX1BP1 and subjected to mitophagy in the presence or absence of the
146 proteasomal inhibitor MG132 (**Fig. S1**). Here, while endogenous TAX1BP1 was not reduced
147 after short depolarization (2 h CCCP), a slight reduction of overexpressed TAX1BP1 levels
148 was observed at this early time point (**Fig. S1**). Importantly, proteasome inhibition did not
149 stabilize poly-ubiquitinated TAX1BP1, neither in the endogenous or overexpressed form,
150 contrary to what was observed for the known proteasome target MFN1 (mitofusin 1) (**Fig.
151 S1**). Thus, the rapid TAX1BP1 ubiquitination observed in this study, seemed to not be part
152 of the initial proteasome-targeting ubiquitination program of OMM-associated proteins, but
153 rather appears to be a regulatory PTM of TAX1BP1.

154 ***Ubiquitinated TAX1BP1 is enriched in depolarized mitochondria***

155 Mitochondria depolarization triggers the activation of parkin-dependent ubiquitination of
156 mitochondrial proteins that will be recognized by the ubiquitin binding domains of autophagy
157 receptors for further successful delivery of mitochondrial cargo to autophagosomes [19]. As
158 expected, endogenous TAX1BP1 translocated to mitochondria after depolarization (**Figure**
159 **2A**). To investigate if the ubiquitinated form of TAX1BP1 was also present on mitochondria,
160 sucrose fractionation experiments were performed. After sucrose fractionation,
161 mitochondrial proteins (i.e: TOM20, VDAC and CS [citrate synthase]) were highly enriched
162 in the mitochondria fraction (MTF) (**Figure 2B**). Under no stress conditions, TAX1BP1 was
163 enriched in the membrane fraction (MMF), suggesting that TAX1BP1 could localize directly
164 to membranous compartments under basal conditions. However, upon short mitochondrial
165 depolarization, TAX1BP1 was enriched in the MTF, also in the ubiquitinated form (**Figure**
166 **2B**). These data indicated that ubiquitinated TAX1BP1 localized on depolarized
167 mitochondria where it may contribute to parkin-dependent mitophagy.

168

169 ***Loss of the TAX1BP1 ubiquitinatable domain reduces clearance of ubiquitinated TOM20***

170 TAX1BP1 is one of the autophagy receptors capable of recognizing ubiquitinated
171 mitochondria and triggering its selective degradation during PINK1/parkin mitophagy [19].
172 However, among the identified five selective autophagy receptors involved in mitophagy,
173 OPTN, NDP52 and TAX1BP1 are characterized as the only ones capable of inducing
174 mitophagy on their own, with TAX1BP1 being the least efficient of the three [11]. Our results
175 are in accordance with the hypothesis of TAX1BP1 having a minor role amongst other

176 autophagy receptors, as siRNA mediated knock-down of TAX1BP1 in WT-parkin HeLa cells
177 did not abolish the degradation of the outer mitochondrial proteins TOM20 and VDAC (**Fig.**
178 **S2A**). On the other hand, overexpression of TAX1BP1 had a positive effect on mitophagy,
179 as we observed an increased mitochondrial clustering upon short depolarization (**Fig. S2B**).
180 These results confirmed the involvement of TAX1BP1 in parkin-mediated mitophagy and
181 strengthened the notion of TAX1BP1 having a minor role when all other autophagy receptors
182 are present. Thus, in order to be able to characterize TAX1BP1 functionality isolated in a
183 null autophagy receptor background, HeLa cells lacking all five major autophagy receptors
184 were used (from now on, referred as 5KO HeLa) [11].

185 To understand the relevance of the identified TAX1BP1 ubiquitination events, lysine
186 substitution (TAX1BP1^{K549R}) and deletion (TAX1BP1ΔCC3) mutants were generated
187 (**Figure 3A**). Here, 5KO HeLa cells were transiently co-transfected with WT-parkin
188 combined with the indicated TAX1BP1 mutants and mitophagy was induced via CCCP-
189 mediated depolarization at the indicated time points. Upon co-expression of WT-parkin and
190 WT or TAX1BP1^{K549R} after early mitochondrial depolarization (4 h CCCP), TAX1BP1
191 ubiquitination was observed, even in the absence of all other four complementary autophagy
192 receptors (**Figure 3B**). In contrast, ubiquitination was reduced upon expression of
193 TAX1BP1ΔCC3 under the same conditions (**Figure 3B-C**). Likewise, TAX1BP1ΔCC3
194 ubiquitination was significantly reduced in 5KO HeLa stably expressing parkin (from now
195 on 5KO-PRKN HeLa) (**Figure 3D-E**). In ubiquitin pulldown experiments with 5KO-PRKN
196 cells, positive controls such as Ub-TOM20, pS65-Ub and total-Ub were captured upon short
197 CCCP-mediated depolarization but not under basal or control bead conditions (**Figure 3D**).
198 Importantly, when analyzing TAX1BP1 ubiquitination status in pulldown experiments,

199 additional higher molecular bands were observed for both WT and TAX1BP1^{K549R}, while
200 only a residual smear after long exposure was observed for TAX1BP1ΔCC3 (**Figure 3D**).
201 Further quantification of these identified higher molecular bands after long TAX1BP1
202 exposure revealed a significant ubiquitination reduction in TAX1BP1ΔCC3 only (**Figure**
203 **3E**). While we cannot discard that residual ubiquitination also occurs in TAX1BP1ΔCC3 -as
204 it is evidenced by the residual smear observed upon depolarization-, a reduced ubiquitination
205 signal is observed in TAX1BP1ΔCC3 when similar TAX1BP1 intensity bands are compared
206 (**Figure 3D**, red vs. blue arrowheads), and this effect is further confirmed upon quantification
207 (**Figure 3E**). The effects observed for TAX1BP1ΔCC3, contrast with the ubiquitination
208 status observed for TAX1BP1^{K549R}, which did not show any significant difference when
209 compared to WT (**Figure 3D-E**). Overall, these data indicate that most of the TAX1BP1
210 ubiquitination events observed upon mitochondria depolarization were localized at the CC3
211 domain of the autophagy receptor, but were not restricted to K549. It is important to note that
212 the CC3 domain of TAX1BP1 is particularly lysine-rich compared to CC1 or CC2 and that
213 the lysines encoded in the CC3 domain of TAX1BP1 are highly conserved across species
214 (**Fig. S3**). Thus, it is very possible that the sole substitution of a single lysine (i.e: K549R) in
215 this domain is not enough to have an impact on the total TAX1BP1 ubiquitination levels, as
216 many other lysines could be alternatively ubiquitinated in this condition.

217 Next, we focused on investigating if and how the ubiquitination status of TAX1BP1 could
218 affect the degradation of specific mitochondrial proteins. For this purpose, we quantified
219 protein levels of the outer and inner mitochondrial proteins: TOM20, VDAC, CS and COX4
220 (cytochrome c oxidase subunit 4I1) upon co-expression of WT-Parkin and the different
221 TAX1BP1 mutants after CCCP-mediated depolarization. Under control conditions, where

222 neither TAX1BP1 nor parkin were expressed, protein levels of all analyzed proteins (VDAC,
223 TOM20, CS and COX4) were not significantly reduced after 4 h of CCCP (**Figure 3B and**
224 **3F-I**). As expected, upon expression of parkin alone or together with WT TAX1BP, an
225 increase in OMM protein degradation was observed (i.e: TOM20 and VDAC) while inner
226 mitochondrial proteins (COX4 and CS) remained unaffected after 4 h of CCCP, when
227 compared to empty controls (**Figure 3F-I**). These results are in agreement with previous
228 studies indicating that the degradation of inner mitochondrial targets in a parkin-expressing
229 HeLa cell model, require longer depolarization exposure [9,17]. Expression of
230 TAX1BP1^{K549R} did not have any impact on VDAC or TOM20 degradation (**Figure 3F-G**).
231 VDAC degradation was increased upon addition of WT or any TAX1BP1 mutant, when
232 compared to parkin transfection alone. However, changes were found to not be significant,
233 suggesting that the autophagy receptor may not be required for the elimination of this
234 particular OMM protein (**Figure 3B and F**). Similarly, no significant changes in TOM20
235 degradation were observed upon TAX1BP1 over-expression, as TOM20 degradation was
236 already enhanced with parkin overexpression alone (**Figure 3B and G**), in agreement with
237 previous studies [11]. However, despite no observed changes in protein degradation under
238 these conditions, a significant increase in Ub-TOM20 was identified in TAX1BP1ΔCC3
239 (**Figure 3G and J**). Thus, these data suggest that the loss of the CC3 ubiquitinatable domain
240 on TAX1BP1 (TAX1BP1ΔCC3) has an impact on the targeting of ubiquitinated TOM20,
241 potentially delaying TOM20 degradation.

242

243

244 ***Modulation of the ubiquitination pattern of TAX1BP1 has mild effects on its translocation***
245 ***behavior to mitochondria***

246 The engulfment of mitochondrial material inside autophagosomes is a step that depends on
247 autophagy receptor functionality and that allows: (i) the recognition of ubiquitinated
248 mitochondrial proteins and (ii) the recruitment of autophagy effectors, which will promote
249 autophagosome biogenesis and eventually allow cargo engulfment [20]. Considering this, we
250 hypothesized that the slight defects observed in mitochondrial degradation could be due to a
251 delay in the TAX1BP1-dependent recognition of mitochondrial material. For this purpose,
252 TAX1BP1 translocation behavior and mitochondria clustering were analyzed.

253 First, basic immunofluorescence was used to visualize TAX1BP1 translocation on
254 mitochondrial material upon co-expression of WT-parkin (**Figure 4A and Fig. S4A**). Under
255 basal conditions, puncta-like structures were observed for all three TAX1BP1 constructs
256 (**Fig. S4A**). Short mitochondria depolarization induced the translocation of all three
257 TAX1BP1 constructs (**Figure 4A**), indicating that both TAX1BP1^{K549R} and TAX1BP1ΔCC3
258 were capable of recognizing depolarized mitochondria. However, TAX1BP1ΔCC3
259 translocation to mitochondria was rather localized in specific regions of the SSBP1 cluster
260 and, unlike parkin translocation, did not co-localize with most of SSBP1 material in some
261 cases (**Figure 4A, zoom panel iv**).

262 Next, mitochondrial morphology analysis was performed by quantifying mitochondria area
263 after depolarization. In this case, given that matrix protein degradation was not significantly
264 affected after short depolarization (**Figure 3B and H**), the matrix protein SSBP1 was used
265 for mitochondrial area quantification by using CellProfiler as previously performed [21].

266 Here, after short depolarization and co-expression of parkin with WT TAX1BP1, we
267 observed a strong reduction of SSBP1 area when compared to control conditions, indicative
268 of mitochondrial clustering and successful mitophagy (**Fig. S4B**). Importantly, while a
269 reduction of mitochondrial area was also observed with parkin expression only,
270 mitochondrial clustering was not as prominent as when WT TAX1BP1 was co-expressed
271 (**Fig. S4B**), indicative of delayed or impaired mitophagy in absence of the autophagy
272 receptor. When analyzing mitochondrial clustering upon co-expression of WT and mutant
273 TAX1BP1, an increase in SSBP1 area and perimeter was observed for TAX1BP1ΔCC3
274 while no changes were observed for TAX1BP1^{K549R} (**Figure 4B-D**). These data indicated
275 that TAX1BP1ΔCC3 had a delayed efficacy in promoting mitophagy.

276 Above results seem to indicate that the recognition of depolarized mitochondria is not
277 impaired by any of the mutants, as both TAX1BP1^{K549R} and TAX1BP1ΔCC3 were co-
278 localizing with mitochondrial material upon depolarization (**Figure 4A**). However, upon
279 expression of TAX1BP1ΔCC3 and short depolarization, we observed an increase in Ub-
280 TOM20 (**Figure 3B and J**) as well as a general delay in mitochondrial clustering, indicated
281 by an increase in SSBP1 foci area and perimeter (**Figure 4B-D**). Additionally, a partial
282 TAX1BP1 translocation to specific SSBP1 cluster regions was observed (**Figure 4A, zoom**
283 **panel iv**). Thus, we hypothesized that the observed TAX1BP1ΔCC3 delay in mitophagy
284 progression may be related to TAX1BP1 capability to recognize SSBP1 clusters. For this
285 purpose, the distribution of TAX1BP1 on depolarized mitochondria material was analyzed
286 with CellProfiler. In general, all TAX1BP1 constructs seemed to recognize SSBP1 material
287 in a similar manner, with distribution percentages ranging from 35-45% of SSBP1 area (**Fig.**
288 **S4C**). While no significant differences were observed between WT and TAX1BP1 mutants,

289 a slight reduction of the mitochondrial area recognized by TAX1BP1ΔCC3 was observed,
290 when compared to WT and TAX1BP1^{K549R} (**Fig. S4C**). To exclude that the observed
291 differences in TAX1BP1 mitochondrial distribution could be due to distinct mitophagy
292 progression stages, parkin distribution on mitochondrial material was additionally analyzed.
293 In this case, no overall differences were observed upon transfection of WT or TAX1BP1
294 mutants, as parkin-dependent recognition of SSBP1 area was found between 60-65% for all
295 cases (**Fig. S4D**). We additionally monitored the percentage of total TAX1BP1 involved in
296 the recognition of depolarized mitochondria. Here, no differences were observed for WT and
297 TAX1BP1 mutant, showing 45-50% of total TAX1BP1 to be engaged with depolarized
298 mitochondria (**Fig. S4E**). We further hypothesized that the differences of TAX1BP1
299 distribution on SSBP1 foci could be caused by differences in TAX1BP1 capability to
300 translocate to mitochondria. For this purpose, the recognized SSBP1 area (X) was plotted
301 against the percentage translocated TAX1BP1 on mitochondria (Y) and correlation analyses
302 were performed for each condition. Indeed, a significant correlation was observed for WT
303 TAX1BP1, with increasing TAX1BP1 being able to recognize 40-50% of SSBP1 area,
304 followed by a TAX1BP1 translocation decrease covering up to 60-80% of SSBP1 area
305 (**Figure 4E**). Correlation analysis was also significant for TAX1BP1^{K549R}, which behaved
306 similarly as WT but with an increased variability on the percentage of translocated
307 TAX1BP1^{K549R} (Y axis), after reaching a maximum of 70% translocated TAX1BP1 (**Figure**
308 **4E**). Surprisingly, unlike for WT and TAX1BP1^{K549R}, no significant correlation was
309 observed for TAX1BP1ΔCC3 (**Figure 4E**). These data suggested an inefficient capability of
310 TAX1BP1ΔCC3 to actively translocate to depolarized mitochondria and thus, distinct
311 binding behavior in comparison to WT TAX1BP1. Additionally, to discard that the
312 differences observed could be due to upstream differences in parkin translocation, a similar

313 correlation analysis was performed for parkin (**Fig. S4F**). Here, significant correlation was
314 found in all cases and no drastic differences were observed for parkin translocation upon
315 expression of all three TAX1BP1 constructs (**Fig. S4F**). In this case, approximately >80% of
316 SSBP1 was found recognized by parkin (**Fig. S4F**), indicating a comparable parkin
317 translocation and thus a similar mitophagy progression stage for all three TAX1BP1
318 expression cases.

319 Next, to validate the previously observed differences in TAX1BP1ΔCC3 binding behavior
320 in a context of stable parkin expression, TAX1BP1 mutants were transfected in 5KO-PRKN
321 HeLa cells and TAX1BP1 translocation was analyzed after 4 h of CCCP treatment. To
322 confirm mitophagy progression was at an advanced level, only cells with mitochondrial
323 COX4-positive clusters were taken into account. Here, cells were classified based on
324 TAX1BP1 translocation to mitochondria (complete vs. localized distribution) (**Figure 4F**).
325 Interestingly, a significant increase of cells with localized TAX1BP1 recognition was
326 observed under conditions of TAX1BP1^{K549R} and TAX1BP1ΔCC3 when compared to WT
327 (**Figure 4F**). These data indicated that the recognition of depolarized mitochondria was
328 slightly impaired in TAX1BP1^{K549R} and TAX1BP1ΔCC3 (**Figure 4E and F**).

329

330 ***Blocking autophagy flux in TAX1BP1ΔCC3 promotes the formation of enlarged***
331 ***TAX1BP1 structures***

332 Next, we sought to examine if the observed differences in mitophagy progression and binding
333 behavior of TAX1BP1^{K549R} and TAX1BP1ΔCC3 would translate in the capability of the
334 autophagy receptor to promote complete elimination of mitochondria. For this purpose,

335 mitochondrial degradation after extended depolarization was analyzed in 5KO-PRKN HeLa
336 cells transfected with WT and TAX1BP1 mutants. Interestingly, all TAX1BP1 constructs
337 were able to induce mitochondria degradation after extended CCCP treatment, as an
338 increased number of cells without mitochondria were observed in comparison to control
339 conditions (**Figure 5A and C**). However, when blocking the autophagy flux with
340 bafilomycin A (BafA), we could observe the presence of small and enlarged TAX1BP1^{+}
341 structures co-localizing with the matrix protein SSBP1 (**Figure 5B**). Importantly, the
342 percentage of cells harboring enlarged TAX1BP1^{+} structures was significantly higher in
343 TAX1BP1ΔCC3 compared to WT or TAX1BP1^{K549R} (**Figure 5D**). In addition, TAX1BP1
344 ubiquitination status at that time point was validated by means of western blotting. Here, in
345 accordance to what was observed at an earlier stage of mitophagy (**Figure 3B**), ubiquitination
346 of TAX1BP1 was conserved upon autophagy flux blockage for WT and TAX1BP1^{K549R},
347 while a strong ubiquitination reduction was seen for TAX1BP1ΔCC3 under these conditions
348 (**Figure 5E**).

349 To confirm that the observed phenotype was not derived from CCCP side effects, additional
350 experiments were performed using a combination of Oligomycin and Antimycin A (OA) in
351 addition to the CCCP treatment (**Figure 5F-G and Figure S5).** Here, similarly as observed
352 in previous experiments, we could identify an increase in TAX1BP1ΔCC3 puncta size when
353 compared to WT or TAX1BP1^{K549R} under both treatment conditions (**Figure 5F**).
354 Importantly, the identified TAX1BP1ΔCC3 enlarged puncta were positive for HSP60
355 (**Figure 5G).** In addition, while TAX1BP1 puncta size significantly increased upon
356 depolarization for both WT and TAX1BP1 mutants, no size differences were observed under
357 BafA control conditions among WT TAX1BP1 and mutants (**Figure S5A-B**).

358 Next, CellProfiler was used to stratify TAX1BP1 puncta according to their size into enlarged,
359 intermediate or small puncta (**Figure S5C and D**). Such unbiased classification confirms the
360 previous eye-based quantification results (**Figure 5D**). Consistently, an increased
361 intracellular percentage of enlarged TAX1BP1 puncta was observed under TAX1BP1ΔCC3
362 expression (**Figure S5E**). Following TAX1BP1 puncta size-stratification, cells with more
363 than 25% of enlarged TAX1BP1 puncta were quantified upon CCCP and OA depolarization
364 (**Figure 5H**). Here, a significant increase of cells with enlarged TAX1BP1ΔCC3 puncta was
365 observed under CCCP treatment, while a less prominent increase was identified under OA
366 conditions (**Figure 5H**).

367 Overall, these data suggested that, while TAX1BP1ΔCC3 was able to promote mitochondria
368 elimination as TAX1BP1^{K549R} and WT TAX1BP1 after long depolarization, the degradative
369 mechanisms driven by TAX1BP1ΔCC3 could differ, as its expression induces a significantly
370 higher prevalence of enlarged TAX1BP1^{+} structures carrying mitochondrial material.

371

372 ***Enlarged TAX1BP1ΔCC3 structures are not simple autophagosomes***

373 Given the fact that TAX1BP1 is considered the least effective autophagy receptor to be able
374 to initiate mitophagy on its own in a 5KO-HeLa cell model [11], it was tempting to speculate
375 that the enlarged TAX1BP1^{+} structures carrying mitochondrial material could be indicative
376 of mitochondrial degradation occurring via a distinct autophagy pathway. Thus, several
377 markers were used to investigate the nature of these enlarged TAX1BP1^{+} structures.
378 Mitochondrial material was identified by using the matrix markers SSBP1 or HSP60 (60 kDa
379 heat shock protein, mitochondrial). As BafA is known to inhibit autophagic flux, the first

380 marker to test was the autophagosome marker LC3B. The enlarged TAX1BP1^{+} HSP60^{+}
381 structures of WT, TAX1BP1^{K549R} and TAX1BP1ΔCC3 were LC3B^{+} (**Figure 6A**). In all
382 cases, these structures seemed to be of a more complex nature, as they were composed of
383 multiple LC3B^{+} entities structures across the Z plane (**Figure 6B, Fig. S6 and**
384 **Supplementary videos1-4**). These results suggest the enlarged TAX1BP1^{+} structures were
385 formed by an accumulation of multiple autophagosomes (**Figure 6B, Fig. S6 and**
386 **Supplementary videos1-4**). On the other hand, all small TAX1BP1^{+} HSP60^{+} structures were
387 engaged in single cup-shaped LC3B^{+} rings, suggesting they were indeed individual
388 autophagosomes (**Figure 7A**).

389 Later steps of autophagy-mediated degradation rely on the fusion of sealed autophagosomes
390 with lysosomes [19]. However, prior to autophagosome-lysosome fusion, autophagosome
391 maturation takes place and sealed autophagosomes may additionally fuse with endosomes,
392 generating a new degradative vesicles termed amphisome [22]. Thus, we decided to prove
393 for the late endosomal marker RAB7 (RAB7A, member RAS oncogene family), the member
394 of the retromer complex VPS35 (which is mutated in rare forms of PD) and the late
395 endosomal and marker CD63/LAMP-3 (CD63 antigen or Lysosomal-associated membrane
396 protein 3). Surprisingly, all enlarged TAX1BP1^{+} structures carrying mitochondrial material
397 were surrounded by RAB7 and VPS35 signals, suggesting additional vesicles were engulfing
398 the identified accumulated LC3B^{+} TAX1BP1^{+} HSP60^{+} structures (**Figure 6C and D**). These
399 patterns contrasted with the ones observed for CD63, which rather seemed to be part of the
400 cargo (**Figure 6E**). On the other hand, all regular sized TAX1BP1^{+} structures were positive
401 for all tested endolysosomal markers (**Figure 7B-D),** with the only particularity that the
402 VPS35 and RAB7 rings engulfed single HSP60^{+} and TAX1BP1^{+} structures. These data

403 indicate that the enlarged TAX1BP1$^+$ structures are vesicles of endolysosomal nature filled
404 with multiple autophagosomes carrying mitochondrial cargo (amphisomes), while the
405 regular-sized TAX1BP1$^+$ structures correspond to individual vesicles or mature
406 autophagosomes.

407

408 ***Enlarged TAX1BP1ΔCC3$^+$ vesicles were also observed in parental HeLa cells with all***
409 ***other complementary autophagy receptors***

410 To confirm the relevance of the previously described phenotype in 5KO-PRKN HeLa cells,
411 similar experiments were performed in WT-Parkin HeLa cells endogenously expressing all
412 other complementary autophagy receptors (NDP52, OPTN, NBR1, SQSTM1/p62,
413 TAX1BP1) (**Fig. S7A**) [11]. Here, siRNA-based transient knockdown experiments were
414 followed by re-transfection of the desired TAX1BP1 constructs and subsequent CCCP-
415 mediated depolarization combined with BafA (**Figure 8A**). Confirmation of efficient
416 silencing was additionally performed via protein expression of total TAX1BP1 (**Figure 8A,**
417 **lower panel**). Overall, TAX1BP1 puncta in all conditions co-localized with the
418 mitochondrial marker HSP60 (**Figure 8A**). Surprisingly, the mean size of all observed
419 TAX1BP1$^+$ puncta per cell significantly increased upon siRNA knockdown and further
420 TAX1BP1 re-transfection in comparison to controls (**Figure 8B**). Indeed, when classifying
421 TAX1BP1 puncta size between small (<50 px^2), intermediate (≤150 px^2) or enlarged (> 150
422 px^2) (**Fig. S7B and C**), the majority of TAX1BP1$^+$ puncta were of small or intermediate
423 sizes, while larger puncta represented a much reduced percentage of the total TAX1BP1$^+$
424 puncta in all conditions (**Fig. S7C**). Of note, there was a 2-fold significant increase of the

425 intracellular percentage of larger TAX1BP1ΔCC3^{+} puncta in comparison to WT TAX1BP1
426 conditions, reaching 5% of total TAX1BP1ΔCC3^{+} puncta identified (**Figure 8C**). An
427 additional increase of the percentage of larger puncta profiles was observed upon WT
428 TAX1BP1 transfection when compared to transfection and silencing controls, suggesting the
429 overexpression of TAX1BP1 could increase its puncta size (**Figure 8C**). Furthermore, while
430 the number of cells with large TAX1BP1^{+} puncta was slightly higher in TAX1BP1ΔCC3 in
431 comparison to re-transfected WT or TAX1BP1^{K549R}, the differences were only significant
432 when compared to siRNA controls (**Figure 8D**). Consistent with previous experiments in
433 5KO-PRKN Hela, TAX1BP1^{+} enlarged puncta also co-localized with the mitochondrial
434 proteins HSP60 in WT-Parkin HeLa (**Figure 8A**). Next, to relate TAX1BP1 mitochondrial
435 removal efficiency upon expression of the different TAX1BP1 constructs in WT-Parkin
436 HeLa, co-localization analysis of HSP60 and TAX1BP1 was performed. First, the percentage
437 of HSP60 foci co-localizing with TAX1BP1^{+} puncta of all sizes was analyzed (**Figure 8E**).
438 An increased percentage of HSP60 co-localizing with TAX1BP1 was observed upon
439 silencing and TAX1BP1 re-transfection in comparison to controls, with no significant
440 differences among all three TAX1BP1 conditions (**Figure 8E**). These data indicated that all
441 TAX1BP1 constructs enhanced the recognition of HSP60 material, in agreement with
442 previous experiments where overexpression of TAX1BP1 had a positive effect on
443 mitochondrial degradation (**Fig. S2B and C**). Next, HSP60 foci co-localizing with enlarged
444 TAX1BP1^{+} puncta were analyzed (**Figure 8F**). Here, while there was a slight increase of the
445 percentage of HSP60 foci recognized by enlarged TAX1BP1ΔCC3^{+} puncta, no significant
446 differences were found among WT and mutants under silencing conditions (**Figure 8F**).
447 However, it is worth noting that the mean area of the identified HSP60 foci co-localizing
448 with TAX1BP1ΔCC3 and TAX1BP1^{K549R} were larger than the ones observed in WT or

449 control conditions, while no differences were observed for WT compared to controls (**Figure**
450 **8G**).

451 In short, we observed an increased prevalence of enlarged TAX1BP1ΔCC3 structures
452 capable of recognizing increased amounts of HSP60 in comparison to WT. Similarly,
453 TAX1BP1^{K549R} enlarged structures are able to engage with increased amounts of HSP60,
454 however the prevalence of TAX1BP1^{K549R} enlarged structures is less abundant than
455 TAX1BP1ΔCC3, suggesting a milder phenotype for the site-substitution mutant. Thus, these
456 data indicated that the enlarged TAX1BP1ΔCC3^{+} structures observed in 5KO-PRKN HeLa
457 cells were of dominant nature, despite the partial rescue observed in WT-parkin HeLa, where
458 all complementary autophagy receptors are present.

459

460 ***Reduced autophagosome formation in TAX1BP1ΔCC3***

461 Next, we hypothesized that the observed accumulation of enlarged amphisomes in
462 TAX1BP1ΔCC3 upon autophagy blockage could be due to defects in autophagy initiation
463 flux at earlier stages. In order to check this, short mitochondria depolarization was induced
464 by CCCP or OA treatment and co-localization of TAX1BP1 and LC3B on mitochondria was
465 further analyzed.

466 As expected, TAX1BP1-HSP60 co-localization upon CCCP or OA depolarization was
467 significantly increased when compared to control conditions (**Figure 9A and Fig. S8A-B**).
468 However, while all TAX1BP1 mutants were able to translocate to mitochondria upon
469 depolarization, a significant reduction on TAX1BP1-HSP60 overlap was observed for

470 TAX1BP1ΔCC3 while no changes in intensity correlation were detected (**Figure 9B-C**).
471 These data are in agreement with previous experiments where we observed a decrease in
472 TAX1BP1ΔCC3 overlap on $COX4^+$ or $SSBP1^+$ mitochondrial material (**Figure 4E-F**).
473 Along those lines, mitochondrial area was found increased in TAX1BP1ΔCC3 upon CCCP
474 treatment only (**Fig. S8C-D**), in agreement with previous experiments (**Figure 4B-D**).

475 Next, to further understand the potential defects in TAX1BP1ΔCC3-dependent autophagy
476 initiation, LC3B colocalization with HSP60 was analyzed (**Figure 9D-E** and **Fig. S8E**). As
477 expected, LC3B-HSP60 overlap upon CCCP or OA depolarization was significantly
478 increased when compared to control conditions (**Figure S8E**). On the other hand, no changes
479 in LC3B overlap with mitochondria were observed for any of the mutants in comparison to
480 WT TAX1BP1 (**Figure 9D**). However, there were significant changes in LC3B-HSP60
481 signal correlation for both TAX1BP1 mutants, as a significant increase in LC3B-HSP60
482 intensity correlation was observed for TAX1BP1ΔCC3 under both CCCP and OA
483 depolarization (**Figure 9E**). Changes in $TAX1BP1^{K549R}$ were only significant under OA
484 treatment conditions (**Figure 9E**). Importantly, this was not a result of increased LC3B
485 intensity in TAX1BP1ΔCC3, as we observed a significant decrease in LC3B intensity for
486 both TAX1BP1 mutants in all conditions (**Figure 9F** and **Fig. S8F**). Similarly, there were
487 also important changes on the LC3B signal area (**Figure 9G**). As expected, TAX1BP1
488 expression alone induced a significant increase in LC3B area and this was accentuated upon
489 mitochondria depolarization (**Fig. S8G**). However, such increase was not as pronounced in
490 TAX1BP1ΔCC3 after depolarization, as we observed a significant reduction of the total
491 LC3B area in TAX1BP1ΔCC3 when compared to WT TAX1BP1 under both CCCP and OA
492 treatment conditions (**Figure 9G**).

493 These data strongly suggest that autophagosome formation induced by TAX1BP1ΔCC3 may
494 be compromised due to a reduced recognition of depolarized mitochondria under these
495 conditions, which results in a generally reduced autophagosome production.

496

497 **Mass-spectrometry analysis of TAX1BP1ΔCC3 pulldown reveals defects in**
498 **intracellular trafficking processes**

499 In order to get an idea of the global processes occurring upon TAX1BP1ΔCC3 expression
500 and try to pinpoint specific TAX1BP1 interactors that could be indicative of distinct non-
501 classical autophagic processes, mass-spectrometry analysis of TAX1BP1 precipitates was
502 performed. Here, HIS-tagged TAX1BP1 was co-precipitated under native conditions by
503 means of Ni-NTA pulldown and the pulled down fractions were further analyzed by mass-
504 spectrometry. Both conditions of depolarization only (16 h CCCP) or depolarization
505 combined with autophagic flux inhibition (16 h CCCP + BafA) were analyzed.

506 Identified protein groups and peptides showed a minor increase for cells expressing WT and
507 mutant TAX1BP1 when compared to the empty plasmid (**Fig. S9A-B**). Furthermore,
508 comparisons of the numbers of protein groups connected to mitochondria as well as the
509 autophagy and vesicular transport machineries revealed no sample specific differences (**Fig.**
510 **S9A**). The overall sample correlations were high and principal component analysis indicated
511 that the main differences between samples stemmed from variations between replicates (**Fig.**
512 **S9C-D**). As further quality control of the dataset, the number of identified peptides for
513 TAX1BP1 peptides and protein quantity were investigated. As expected, TAX1BP1 was
514 found to be absent in the control samples (**Fig. S9E-F**). Surprisingly, TAX1BP1^{K549R} quantity

515 values were lower in comparison to WT and TAX1BP1ΔCC3 (**Figure S9F**). Statistical
516 differences were analyzed between TAX1BP1ΔCC3 and WT upon CCCP treatment only
517 (**Fig. S10A and Table S2**) or in combination with BafA (**Figure 10A and Table S1**). Here,
518 when comparing TAX1BP1ΔCC3 with WT after extended depolarization only, an increased
519 co-precipitation of inner mitochondrial proteins was identified (**Fig. S10A**). These findings
520 were in line with the identified delayed mitochondrial degradation phenotype of
521 TAX1BP1ΔCC3 during earlier depolarization (**Figure 4B-D**). On the other hand, when
522 comparing TAX1BP1ΔCC3 and WT upon CCCP combined with BafA inhibition, multiple
523 proteins involved in vesicle-mediated transport, mitophagy or mitochondria localized
524 proteins were significantly regulated (**Figure 10A**).

525 Significantly up- and downregulated proteins were further analyzed for statistical
526 overrepresentation on GO biological processes for the condition of depolarization combined
527 with autophagy flux blockage only, using the panther database (www.pantherdb.org, version
528 19.0) [23]. Upon comparing the protein signatures interacting with TAX1BP1ΔCC3 against
529 WT under CCCP and BafA treatment combined, GO-term analysis indicated a
530 downregulation of several vesicle-related biological processes, some of them related to
531 retrograde transport or vesicle budding. Moreover, an upregulation of DNA replication,
532 repair and translation processes and an additional upregulation of mitophagy response
533 processes related to mitochondria depolarization were identified (**Figure 10B**).

534 When analyzing the protein signatures interacting with TAX1BP1ΔCC3 under these
535 conditions in more detail, a downregulated co-precipitation of TAX1BP1 with several
536 proteins involved in intracellular trafficking was identified (**Figure 10A**). Those included the
537 Rab-GTPases RAB8A, RAB14 and RAB1A, proteins involved in membrane organization

538 (TMEM33 [Transmembrane protein 33], VPS33A [vacuolar protein sorting-associated
539 protein 33A]) and other proteins involved in endosome budding from the Golgi apparatus
540 (ARF1 [ADP-ribosylation factor 1], ARF4 [ADP-ribosylation factor 4]). On the other hand,
541 an upregulated interaction with ubiquitin and inner mitochondrial proteins was found (**Figure**
542 **10A**). This later finding correlated with previous data showing an increased amount of
543 enlarged TAX1BP1ΔCC3 positive vesicles carrying increased amounts of mitochondrial
544 material (**Figure 5A and G and Fig. 8G**) as well as with the presence of Ub-TOM20 after
545 short depolarization (**Figure 3B and J**). Additionally, several vesicular-trafficking related
546 proteins were identified to increasingly co-precipitate with TAX1BP1ΔCC3. Those were:
547 three COPII vesicle-related proteins (SEC31A, SEC24D and SEC24A [protein transport
548 protein Sec24A/D/31A]) [24]; the endocytosis-related protein EPN1 (epsin-1) [25]; ERC1
549 (ELKS/Rab6-intercting/CAST family member 1) known to be involved in exocytosis
550 [26,27]; and the GTPase activating protein ACAP2 (Arf-GAP with coiled-coil, ANK repeat
551 and PH domain-containing protein 2), involved in endosomal trafficking [28] (**Figure 10A**).
552 Moreover, at a lower significance level (p-value<0.1), an upregulation of autophagy-related
553 protein WDR45B/WIPI3 (WD repeat domain phosphoinositide-interacting protein 3) as well
554 as the Rab7 GTPase activator TBC1D15 (TBC1 domain family member 15) were identified
555 (**Figure 10A**), both also implicated in mitophagy or general autophagy [29–32]. Importantly,
556 no significant interaction with ubiquitin or vesicle-related proteins was observed for
557 TAX1BP1^{K549R} while an additional interaction with mitochondrial proteins was identified
558 (**Fig. S10B and Table S1**).

559 These data indicated that TAX1BP1ΔCC3 under these conditions was capable of
560 dysregulating vesicle-trafficking processes while being able to increasingly interact with

561 ubiquitinated mitochondrial targets. Overall, these findings reinforced the hypothesis that
562 removing the highly ubiquitinatable domain CC3 of TAX1BP1 impaired its mitochondrial
563 targeting efficacy which may additionally have an effect at later stages of autophagy, when
564 autophagosomes are formed and vesicular transport is essential for autophagosome
565 maturation.

566

567 **Discussion**

568 Complete mitochondria elimination during PINK1/Parkin mitophagy is subject to autophagy
569 receptor-dependent recognition of ubiquitinated mitochondria. In this context, five
570 autophagy receptors have been linked to PINK1/parkin mitophagy: NBR1, SQSTM1/p62,
571 OPTN, NDP52 and TAX1BP1 [33]. PTMs are known to play a regulatory role on autophagy
572 receptor functionality during selective autophagy [34]. Here we show that, in a context of
573 PINK1/parkin mitophagy, TAX1BP1 ubiquitination at its CC3 domain can regulate the
574 delivery of depolarized mitochondria to either a classical autophagy-dependent degradative
575 pathway or to an alternative pathway that is more dependent on the endolysosomal
576 machinery, without dramatically compromising the elimination of defective mitochondria.

577 TAX1BP1 ubiquitination at K549 or other lysines within its CC3 domain have been
578 described under similar mitochondria depolarizing conditions as the ones reported in this
579 study (**Figure 1A-B**) [18,35], strongly suggesting a regulatory role for this PTM. Indeed, we
580 could observe that TAX1BP1 ubiquitination did not direct the autophagy receptor for early
581 proteasomal degradation (**Fig. S1A**) but instead, ubiquitinated TAX1BP1 was found enriched
582 in mitochondria fractions upon short depolarization (**Figure 2B**). The limited effects of the

583 K549 point mutation suggests complexity and redundance in the TAX1BP1 ubiquitination
584 pattern. This study relies on the deletion of the whole CC3 domain to understand the role of
585 TAX1BP1 ubiquitination and the data presented here indicate that the CC3 deletion does not
586 impair the overall functionality of the autophagy adaptor. However, we cannot discard that
587 the entire CC3 domain deletion subtly perturbs TAX1BP1 structure, accounting for potential
588 effects beyond ubiquitination. Nevertheless, the CC3 domain is richer in lysins in comparison
589 to the other coiled-coiled regions of TAX1BP1, and the lysines within the CC3 domain are
590 highly conserved across mammalian species (**Fig. S3**). Indeed, when deleting the CC3
591 domain of TAX1BP1, a clear decrease in total TAX1BP1 ubiquitination was observed, both
592 after short (4 h CCCP) and extended depolarization combined with autophagy flux inhibition
593 (16 h CCCP + BafA) (**Figure 3B-E, Figure 5E and Fig. S2C**). Interestingly, when checking
594 TAX1BP1 predicted structure in AlphaFold [36], the structure of the regions connecting the
595 different CC domains and the ubiquitin binding domain (UBD) with the CC3 are of lowest
596 confidence (**Figure 11A**). This could be indicative of a highly dynamic behavior of those
597 regions, which could in turn influence the orientation of the distinct CC and UBD regions.
598 Thus, while there is no evidence for a potential structural interaction between the CC3 and
599 UBD regions based on the AlphaFold model, it is tempting to speculate that the ubiquitination
600 of multiple lysines at the CC3 could influence the orientation or availability of the UBD
601 region (**Figure 11B**).

602 Abolishing TAX1BP1 ubiquitination at CC3 domain by deleting its domain did not impair
603 the degradation of OMM proteins but had a negative impact in the targeting of Ub-TOM20
604 (**Figure 3B, F-J**) and promoted a slower clustering of mitochondria after short depolarization
605 (**Figure 4A-D**). Moreover, while CC3 ubiquitination was proven not essential for TAX1BP1

606 translocation to mitochondria (**Figure 4A**), a lack of it did significantly reduce the
607 distribution of the autophagy receptor on CCCP- and OA-depolarized mitochondria (**Figure**
608 **4E-F and Figure 9A-B**). Thus, suggesting that the delayed mitochondrial degradation and
609 clustering of TAX1BP1ΔCC3 was possibly due to an impairment on depolarized
610 mitochondrial recognition. One of the first reports describing TAX1BP1 domain structure
611 and its first links to immunity-related functions, described three different coiled-coil domains
612 localized between the now known SKITCH and UBA domains [37]. Interestingly, Ling and
613 Goeddel identified the CC1 and CC2 domains to be essential for TAX1BP1
614 homodimerization under basal conditions, while the region flanking the CC3 domain seemed
615 to play a minor role in its assembly [37]. Similarly to TAX1BP1, the autophagy receptor
616 NDP52 also possesses a central CC region recently identified to be crucial for NDP52
617 homodimerization in the context of mitophagy [38,39]. Based on this, it is tempting to
618 speculate that the differences observed in TAX1BP1ΔCC3 distribution on mitochondrial
619 material might be due to a reduced homodimerization capacities. However, given that the
620 recognition of depolarized mitochondria was significantly reduced in TAX1BP1ΔCC3
621 (**Figure 4E-F and 9A-B**) and this phenomenon was accompanied by a reduced formation of
622 $LC3B^{+}$ vesicles, as indicated by a reduced LC3B intensity and total LC3B area in
623 TAX1BP1ΔCC3 (**Figure 9F-G**), it seems possible that the delivery of defective
624 mitochondria in TAX1BP1ΔCC3 could be compromised or delayed from this step on. Along
625 these lines, our study also reveals that, even though the lack of ubiquitination at CC3 does
626 not impair complete mitochondrial degradation (**Figure 5C**), the degradative pathways
627 governing this process may differ between WT and TAX1BP1ΔCC3, as an increased
628 presence of enlarged degradation vesicles was observed in TAX1BP1ΔCC3 only (**Figure 5**
629 **and Fig. S5**), even under conditions where all other autophagy receptors were present

630 (**Figure 8 and Fig. S7C**). It is noteworthy that the here identified enlarged TAX1BP1^{+}
631 vesicles were prominently surrounded by the PD gene product VPS35. These findings may
632 suggest a functional link between the mitophagy pathway regulated by the most common
633 recessive gene products PINK1 and parkin together with the rare VPS35 gene product,
634 suggested to be involved in vesicle trafficking effects of the common dominant PD gene
635 product LRRK2 (Leucine-rich repeat serine/threonine-protein kinase 2). While this latter
636 connection in our work may be quite superficial, recent work by the group of Vandenberghe
637 W. and colleagues has made evident a remarkable functional link between VPS35-LRKK2
638 in the context of PINK1/parkin mitophagy [40]. The authors identify the novel VPS35
639 mutation p.D620N to not compromise the initiation steps of PINK1/parkin mitophagy but
640 significantly impair the recruitment of the autophagy receptor OPTN on depolarized
641 mitochondria [40]. While at this point it still remains yet to be elucidated if TAX1BP1
642 ubiquitination may have any impact on this molecular axis, our mass-spectrometry data
643 seems to confirm defects in vesicular trafficking, as many targets related to vesicle-mediated
644 transport were downregulated in TAX1BP1ΔCC3 (**Figure 10A**). Nevertheless, we could not
645 identify a unique endolysosomal marker specific for the enlarged degradative vesicles only
646 under these conditions, as all enlarged and small vesicles were positive for the same markers
647 (LC3B, VPS35, RAB7 and CD63) (**Figure 6 and Figure 7**). However, it is important to
648 emphasize that strong structural differences were clearly observed between small and
649 enlarged TAX1BP1^{+} degradative vesicles, being the enlarged ones more prevalent in
650 TAX1BP1ΔCC3 than in WT. More precisely, the enlarged TAX1BP1ΔCC3^{+} structures
651 contained numerous TAX1BP1^{+} LC3B^{+} vesicles carrying mitochondrial material (**Figure**
652 **6A-B, Fig. S6 and Supplementary videos 1-4**), where globally surrounded by RAB7^{+} and
653 VPS35^{+} vesicles (**Figure 6C-D**) and were additionally positive for CD63 (**Figure 6E**). On

654 the other hand, small vesicles found in all TAX1BP1 constructs consisted of single
655 TAX1BP1^{+} LC3B^{+} positive vesicles also carrying mitochondrial material and were equally
656 positive for all the tested endolysosomal markers (RAB7, CD63 and VPS35) (**Figure 7**).
657 These data seem to indicate that the degradation pathways involved in WT and ubiquitination
658 deprived TAX1BP1 are possibly of the same nature and the identified enlarged and small
659 vesicles are the result of autophagosomes fused with endosomes (amphisomes) or lysosomes
660 (autolysosomes) [22], potentially indicating that the complex enlarged TAX1BP1 structures
661 might be the result of defects in autophagosome maturation. Autophagosome fusion with
662 endosomes is known to be necessary for autophagosome maturation as it increases the pH of
663 the degradative vesicle and is considered a previous step for lysosome fusion [22]. On the
664 other hand, autophagy flux inhibition via BafA does not specifically hinder the fusion of
665 autophagosomes with lysosomes [41], thus we cannot discard that the observed enlarged
666 TAX1BP1 positive vesicles simply correspond to autolysosomes with more complex LC3B-
667 TAX1BP1-HSP60 cargo. It is important to note that TAX1BP1 has been reported to interact
668 with the cytoskeletal motor MYO6 (unconventional myosin-VI), known to be involved in
669 endocytic transport and to facilitate autophagosome maturation by interacting with the UBD
670 of TAX1BP1 [42]. Interestingly, compromising autophagosome maturation via transient
671 knock-down of MYO6, induced the formation of immature enlarged autophagosomes
672 positive for SQSTM1/p62 [42]. Another recent example of the relationship between
673 degradative vesicle size and endosome/autopagosome maturation was achieved by transient
674 knockdown of individual HOPS complex subunits, known to play an essential role in
675 endosome and autophagosome fusion with lysosomes [43]. Based on this, it seems reasonable
676 to think that the enlarged vesicles observed in TAX1BP1ΔCC3 are the result of impaired

677 autophagosome maturation driven by TAX1BP1ΔCC3 alone and further accentuated by
678 BafA treatment.

679 Additionally, it is important to emphasize that the formation of enlarged degradative vesicles
680 was not only observed in 5KO HeLa (**Figure 5B-D, F-H and Figure 6**) but also in parental
681 WT-Parkin HeLa with all complementary autophagy receptors (**Figure 8**). In this case, the
682 observed TAX1BP1ΔCC3 positive structures were generally smaller as the ones observed in
683 5KO HeLa. However, amongst the regularly sized TAX1BP1 positive structures, an
684 increased proportion of enlarged TAX1BP1ΔCC3 positive structures was observed (**Figure**
685 **8C-D**). These data indicate that while the presence of complementary autophagy receptors
686 can partially compensate for the observed phenotype, the TAX1BP1ΔCC3 dependent
687 formation of enlarged degradative vesicles can be considered of a dominant nature.
688 Moreover, the mitochondrial material recognized by the TAX1BP1^{+} enlarged vesicles was
689 significantly increased in TAX1BP1ΔCC3 and TAX1BP1^{K549R} in comparison to WT (**Figure**
690 **8G**), strongly suggesting a decreased efficiency of ΔCC3, also under conditions of
691 complementary autophagy receptor expression. Thus, as larger TAX1BP1 vesicles were
692 observed in 5KO HeLa when compared to the ones seen in WT-Parkin HeLa, it seems
693 reasonable to think that the expression of complementary autophagy receptors can partially
694 compensate for the TAX1BP1-dependent formation of enlarged degradative vesicles. This is
695 in agreement with previous reports indicating TAX1BP1 as the least efficient autophagy
696 receptor to promote PINK1/parkin mitophagy in 5KO HeLa [11]. In addition, recent reports
697 using proximity-labelling approaches have indicated that TAX1BP1 can interact with other
698 autophagy receptors during mitophagy [44,45] suggesting the cooperation with more

699 efficient autophagy receptors could partially compensate for the observed phenotype in 5KO
700 HeLa.

701 Upon general GO-Term analysis of TAX1BP1ΔCC3 native pulldown (**Figure 10B**), a
702 significant decrease in interactions related to general vesicle trafficking was identified and is
703 in agreement with previous results showing an increased presence of TAX1BP1ΔCC3
704 enlarged vesicles under these conditions (**Figure 5B-D, F-H, Figure 6 and Fig. S5**). An
705 upregulated interaction with inner mitochondrial proteins and ubiquitin confirmed a
706 decreased efficiency of ΔCC3 in mitochondria degradation (**Figure 3C, Figure 4B-D and**
707 **Figure 10A**). However, expected TAX1BP1 interactors like RB1CC1/FIP200 (RB1-
708 inducible coiled-coil protein 1) or MYO6 could not be detected for neither of the mutants or
709 WT TAX1BP1. The increased interaction of TAX1BP1ΔCC3 with ubiquitin and the lack of
710 MYO6 co-precipitation may be indicative of delayed ubiquitinated mitochondria recognition,
711 as MYO6 binding is known to compete with ubiquitin at the UBD of TAX1BP1 [42]. On the
712 other hand, an upregulated interaction of TAX1BP1ΔCC3 with the components of COPII
713 vesicle coat complex SEC24A, SEC24D, SEC31A and the receptor-mediated endocytosis
714 EPN1 were identified [46–48] (**Figure 10A**). Similarly, albeit at a lower-significance level,
715 an increased interaction of two autophagy-related proteins involved in autophagosome
716 biogenesis (WDR45B and TBC1D15) was observed (**Figure 10A**). Importantly, COPII
717 vesicles are known to be important source of membrane lipids for the formation of
718 autophagosomes and indeed, recent reports have demonstrated that both SEC24 and SEC31
719 can interact with ATG9 vesicles, directly influencing autophagosome biogenesis [49–51].
720 Similarly, the Rab GTPase activating protein TBC1D15 is closely implicated with mitophagy
721 progression via its capacity to modulate active RAB7 levels at the OMM in favor of

722 autophagosome biogenesis [29,30]. On the other hand, WDR45B/WIPI3 is known to localize
723 at nascent autophagosomes as well as in late endosomes and thus seems to also play a role in
724 autophagosomes biogenesis and maturation [31,32]. Thus, given that TAX1BP1ΔCC3
725 induced (i) a delayed delivery of Ub-TOM20 (**Figure 3J**), (ii) a decrease in mitochondrial
726 clustering as well as a reduced recognition of defective mitochondria (**Figure 4B-F and**
727 **Figure 9B**) and (iii) promoted a reduced sequestration of $LC3B^+$ vesicles upon short
728 depolarization (**Figure 9G**), it seems reasonable to think that the interaction of
729 TAX1BP1ΔCC3 with the autophagosome biogenesis-related proteins at such later stage of
730 the pathway is probably due to a slower capability of the autophagy receptor to recruit
731 autophagy-related proteins in charge of autophagosome biogenesis. Indeed, decreased
732 interactions of TAX1BP1ΔCC3 were observed for the Rab GTPases RAB14, RAB1A and
733 RAB8A, the ER-transmembrane protein TMEM33 and the HOPS complex member VPS33
734 (**Figure 10A**). Rab GTPases are generally involved in endosomal vesicle trafficking but have
735 also been described to play a role in modulating autophagy: RAB1A has been described to
736 be essential for autophagosome formation [52,53] while RAB14 is implicated in
737 autophagosome maturation [53]. Similarly, VPS33A acts as a tether between
738 autophagosomes and lysosomes to facilitate their fusion [22,54]. Potential defects in
739 autophagosome maturation would be in agreement with the identified sustained ubiquitin
740 interaction, considering that MYO6 interaction competes with ubiquitin at the UBD of
741 TAX1BP1 [42]. Overall, our data suggest that the vesicle-trafficking defects identified in
742 TAX1BP1ΔCC3 may be due to impaired autophagosome biogenesis or maturation and likely
743 derive from a reduced recognition of depolarized mitochondria and a reduced sequestration
744 of $LC3B^+$ vesicles at earlier stages of mitophagy (**Figure 12**).

745 **Conclusions**

746 In this study, we identified the CC3 of TAX1BP1 as a highly ubiquitinated region during
747 PINK1/parkin mitophagy which is not essential for complete mitochondria degradation.
748 However, while reducing CC3 ubiquitination did not really have an impact on OMM protein
749 degradation, other important defects related to mitophagy progression were identified: (i)
750 reduced clearance of ubiquitinated TOM20, (ii) reduced mitochondrial clustering and (iii)
751 reduced TAX1BP1 recognition of depolarized mitochondria, which translated in a (iv)
752 localized presence of $LC3B^{+}$ vesicles on depolarized mitochondria. Blocking autophagy
753 under these conditions had a significant impact on vesicular trafficking, as evidenced by the
754 complex architecture of enlarged $TAX1BP1^{+}$ degradative vesicles which were highly
755 prevalent in the absence of the ubiquitinatable CC3 domain. Our data strongly suggest that
756 the identified vesicular trafficking defects may be driven by a delayed initiation of
757 autophagosome biogenesis as well as an impairment with autophagosome maturation and are
758 a reflection of the identified functional changes of TAX1BP1ΔCC3, which relies on an
759 alternative degradation pathway that is substantially more dependent on the endolysosomal
760 machinery (**Figure 12**).

761

762 **Limitations of the study**

763 This study provides evidence for an influence of TAX1BP1 ubiquitination on PINK1/parkin-
764 mediated mitophagy in an idealized, designed HeLa cell culture model. To expand the
765 relevance of the findings provided in this manuscript, more physiological cell models should
766 be investigated, which would require sophisticated manipulations to study if and how

767 TAX1BP1 ubiquitination influences the clearance pathways of defective mitochondria.
768 Given that all the experiments carried out in this study relied on the overexpression of parkin
769 or TAX1BP1 (WT or mutants), future studies carried out for validation should also pay
770 attention on physiologically relevant expression levels of both the E3 ligase and the
771 autophagy adaptor.

772

773 **Materials and methods**

774 Cell culture, treatments and transfections

775 All cell lines were grown at 37°C and 5% CO_2 with high-glucose Dulbecco's modified eagle
776 medium (DMEM). WT-Parkin and 5KO-PRKN HeLa were supplemented with 0.7 mg/ml
777 geneticin (Gibco, 10131-027) to ensure stable parkin expression. HeLa cells stably
778 expressing WT or inactive mutant (C431A) were previously described [55]. To obtain 5KO
779 HeLa stably expressing WT-Parkin (5KO-PRKN HeLa), cells were transfected with BglII
780 linearized pcDNA3.1-3xFlag-Parkin for 24 hours and were further selected with 1.8 mg/ml
781 of Geneticin for 13 days. Upon selection, clones were screened for homogenous Parkin
782 expression. Mitophagy induction was achieved with 10 µM CCCP (Sigma, 555-60-2) for the
783 indicated time points. Proteasome and autophagy inhibition were induced with 10 µM
784 MG132 (Sigma, C2211) or 400 nM BafA (Chemcruz, sc-201550A), respectively. Inhibition
785 treatments were initiated half an hour before CCCP treatment and were maintained in
786 combination with CCCP for the indicated periods. Long CCCP treatment of 5KO-PRKN
787 HeLa was combined with 60 µM Q-VD-Oph (QVD, Selleckchem, S7311) to prevent cell
788 death. Transient transfection of the indicated constructs was performed with FuGENE6®

789 (Promega, E2692), following manufacturer's instructions. HeLa cells were transfected with
790 5 nM of siRNA for three consecutive days using Hiperfect (Qiagen, 301709). The following
791 siRNA were used: negative control (AllStars negative, Qiagen, SI03650318); TAX1BP1_7,
792 5'-CAGATCAATCAGCTAATAATA-3' (Qiagen, SI02781268); TAX1BP1_9, 5'-
793 AAGGGTCTTACTGAAGTAACA-3' (Qiagen, SI03036124); TAX1BP1_8, 5'-
794 CAGTCTTTGGCTTATCAATAA-3' (Qiagen, SI02781296).

795 Expression constructs

796 The construct pcDNA3.1-3xFlag-Parkin has been described previously [56] and was used to
797 transiently express parkin in 5KO HeLa and to generate the stable 5KO-PRKN as previously
798 explained. Full length WT, TAX1BP1^{K549R} and TAX1BP1ΔCC3 cDNA were amplified from
799 commercial vectors obtained from Origene (WT TAX1BP1, RC208233) or eZyvec on
800 demand (K549R and ΔCC3, Quote: D2022-10) and were sub-cloned into pCMV-6HIS vector
801 to ensure equal expression conditions. Obtained constructs were further sequenced prior to
802 use.

803 Western blotting

804 Upon treatment, cells were washed once with phosphate-buffered saline (PBS) and directly
805 harvested. For whole cell lysate samples, cell pellets were resuspended in urea lysis buffer
806 (10 mM Tris, pH 8.0, 100 mM NaH_2PO_4, and 8 M urea) after a short centrifugation step
807 (9727 x g for 1 minute [min] at 4°C). Lysates were passed through a 26-gauge needle to break
808 the DNA for at least 5 times. Whole cell lysate fractions were obtained after pelleting debris
809 at 21885 x g for 15 min at 4°C. Protein concentration was measured using the Bradford
810 Protein Assay Dye Reagent Concentrate (Bio-Rad, 5000006) following manufacturer's

811 instructions. Proteins were separated using 4-12% NuPage (Invitrogen, NP0329BOX), 3-8%
812 Tris-Acetate pre-casted (Invitrogen, EA0378BOX) or self-casted polyacrylamide gels and
813 were run at a fixed voltage of 80-100 V for at least 1,5 hours at room temperature (RT).
814 Proteins were transferred to polyvinylidene fluoride (PVDF) membranes (Merck,
815 IPVH00010) at constant voltage of 25 V for an overnight run or at 100 V for 2 hours,
816 respectively. Upon transfer, membranes were blocked with 5% non-fat dried milk or 5%
817 bovine serum albumin in Tris-buffered saline containing 0.1% Tween-20 (TBS-T).
818 Membranes were incubated with primary antibodies for 2 h at RT or overnight at 4ºC. After
819 three consecutive TBT-T washes of 5 min, membranes were incubated with the
820 corresponding secondary antibodies diluted in 5% of non-fat dried milk for 1 hour at RT.
821 Upon additional three TBT-T washes of 5 min, protein bands were visualized using
822 chemiluminescent-horseradish peroxidase (HRP) substrate (Millipore; WBKLS0500) and
823 Ultracruz autoradiography films (Santa Cruz Biotechnology; sc-201697). The following
824 primary antibodies were used: Actin (1:50000, Sigma Aldrich, A5441), Calnexin (1:10000,
825 Enzo Life Sciences, ADI-SPA-860), CS (1:6000, GeneTex, GTX110624), Flag-tag
826 (1:10000, Sigma-Aldrich, F1804), LAMP1 (1:10000, DSHB Hybridoma bank, Clone
827 H4A3), LC3B (1:10000, GeneTex, GT3612), LC3B (1:10000, Cell signaling, 835065),
828 MFN1 (1:10000, Abnova, H00055669-M04), NBR1 (1:10000, ProteinTech, 16004-1-AP),
829 NDP52 (1:10000, ProteinTech, 12229-1-AP), OPTN (1:10000, Atlas antibodies,
830 HPA003360), SQSTM1/p62 (1:10000, BD Biosciences, 610832), Parkin (1:50000, Cell
831 signaling, 4211S), phospho-Ubiquitin (Ser65) (1:1000, Cell Signaling, 52802), TAX1BP1
832 (1:1000, Novus Biologicals, NBP1-86662), TOM20 (1:30000, Santa Cruz, sc-17764),
833 TOM20 (1:6000, Proteintech, 11802-1-AP), Total Ubiquitin (1:10000, Millipore,
834 MAB1510), VDAC (1:10000, ProteinTech, 66345-1), VDAC (1:30000, Millipore,

835 AB10527), Vinculin (1:50000, Sigma Aldrich, V9131). The following secondary antibodies:
836 Anti-mouse HRP (1:10000, Amersham Pharmacia, 115-035-003), Anti-rabbit HRP
837 secondray (1:10000, Amersham Pharmacia, 111-035-003). Quantification of relative protein
838 levels was obtained via densitometry using ImageJ software. Briefly, individual protein
839 bands were normalized to Vinculin or Actin protein levels.

840 Immunofluorescence

841 HeLa cells were seeded in 0,1 mg/ml PDL (Sigma-Aldrich, P6407) pre-coated round
842 coverslips (Ø: 12 mm). After treatment, cells were fixed with 4% PFA for 20 min. After
843 fixation and three consecutive washes with PBS, permeabilization was performed with 1%
844 Triton-X for 5 min at room temperature (RT). After three washing steps with PBS, blocking
845 was performed at RT for 1 h with 10% fetal bovine serum or donkey serum (blocking buffer).
846 Afterwards, coverslips were incubated with the corresponding primary antibodies diluted in
847 blocking buffer for 2 h at RT. After three washing steps with PBS, coverslips were incubated
848 with secondary antibodies diluted in blocking buffer for 1 h at RT. Following three additional
849 washing steps with PBS, nuclei were stained with 2 µg/ml of Hoechst 33342 in PBS for 5
850 min at RT. After incubation, three additional washing steps with PBS were performed.
851 Coverslips were finally mounted with fluorescent mounting media (Agligent Dako, S3023).
852 Imaging was performed using an AxioImager microscope equipped with Apotome imaging
853 system (Carl Zeiss, Germany). Images were processed with the ZEN 2.3 lite software and
854 Image J. For LC3B immunostaining, cells were fixed with ice-cold methanol for 2-3 min.
855 Further immunostaining steps were performed as previously described. Image acquisition of
856 endogenous LC3B was realized with a Nikon Ti2e spinning disk confocal microscope. In
857 this case, images were processed using the NIS-Elements software (Nikon, Germany). The

858 following primary antibodies were used: CD63 (1:250, Antibodies online, ABIN94214),
859 COX4 (1:10000, Cell signaling, 4850), HIS-tag (1:500, Addgene, 184180), HSP60 (1:1000,
860 Novus Biologicals, NBP3-05536), LC3B (1:500, Cell signaling, 835065), Parkin(1:10000,
861 Cell signaling, 4211S), RAB7 (1:200, Cell signaling, 95746), TAX1BP1 (1:500, Novus
862 Biologicals, NBP1-86662), VPS35 (1:250, Novus Biologicals, NB100-1397). The following
863 secondary antibodies were used: Donkey anti-sheep Alexa Fluor 647 (1:1000, Invitrogen, A-
864 21448), Donkey anti-mouse Alexa Fluor 488 (1:1000, Invitrogen, A-21202), Donkey anti-
865 mouse Alexa Fluor 568 (1:1000, Invitrogen, A-10037), Donkey anti-rabbit Alexa Fluor 488
866 (1:1000, Invitrogen, A-21206), Donkey anti-rabbit Alexa Fluor 568 (1:1000, Invitrogen, A-
867 10042), Donkey anti-chicken Alexa Fluor 647 (1:1000, Invitrogen, A78952), Donkey anti-
868 goat Alexa Fluor 648 (1:1000, Invitrogen, A21447), Donkey anti-goat Alexa Fluor 488
869 (1:1000, Invitrogen, A11055).

870 Eye-based quantification of TAX1BP1 colocalization on COX4 was performed by taking
871 into account only TAX1BP1^{+} cells with COX4 clumps after 4 h CCCP treatment, to account
872 for parkin-positive cells. TAX1BP1 behavior was classified between complete or localized
873 apposition of COX4 clump depending on its distribution. In situations where both TAX1BP1
874 behaviors were observed in the same TAX1BP1^{+} cell, localized apposition of TAX1BP1 with
875 COX4 cluster was considered. Quantification of complete mitochondria elimination upon
876 TAX1BP1 transfection was achieved by only taking into account parkin-positive cells
877 (empty control) or cells positive for both parkin and TAX1BP1 (TAX1BP1 transfection) after
878 CCCP treatment. Cells were considered to be cleared of mitochondria where no SSBP1
879 puncta were observed. Quantification of small or enlarged TAX1BP1 positive structures after
880 extended depolarization combined with BafA inhibition was performed by taking into

881 account only parkin-positive cells. Cells were classified between containing small or
882 enlarged TAX1BP1 structures according size. In situations where both enlarged and small
883 TAX1BP1 structures were observed in the same TAX1BP1^{+} cell, the cell was quantified as
884 containing enlarged TAX1BP1 structures.

885 Mitochondria fractionation

886 Mitochondria purification was performed as described in [57] with some modifications. Cell
887 pellets were first resuspended in mitochondrial buffer (MB) (210 mM mannitol, 70 mM
888 sucrose, 10 mM HEPES, 1 mM EDTA at pH 7.5) and further cell lysis was performed
889 mechanically using a glass homogenizer. After a first lysing series of 30 mechanical stokes,
890 cell homogenates were centrifuged at 600 x g for 10 min 4ºC. The remaining pellet was
891 resuspended with the remaining supernatant and two additional lysing series were performed,
892 with an in-between centrifugation step (600 x g for 10 min 4ºC). After the first and last
893 centrifugation, the remaining supernatant was recovered (corresponds to F1). The remaining
894 pellet was resuspended in 800 µl MB and was centrifuged at 700 x g for 10 min at 4ºC to
895 obtain the crude mitochondria pellet and the second supernatant fraction (F2). Crude
896 mitochondria pellets were resuspended in 250 µl MB and layered into a discontinuous
897 sucrose gradient formed by a 6 ml layer of 1.2 M sucrose over a 5 ml layer of 1.6 M sucrose
898 using ultra-clear tubes (14 x 89mm, Beckmann). Loaded gradients were centrifuged using a
899 Beckman ultracentrifuged equipped with a SW40Ti rotor at 96000 x g for 2 hours at 4ºC
900 (acceleration and deceleration parameters were set to 3). Upon centrifugation, bands of
901 interest were recovered. On the lighter sucrose layer, the band corresponding to membrane
902 fraction (MMF) was collected and at the layer interface, the band corresponding to enriched
903 mitochondria fraction (MTF) was collected. Upon collection, sucrose was diluted with four

904 volumes of MB and all fractions were pelleted at 13000 x g for 10 min at 4ºC. Pellets were
905 resuspended in urea buffer (10 mM Tris, pH 8.0, 100 mM NaH2PO4, and 8 M urea). Equal
906 protein amounts of each fraction were subjected to western blot analysis.

907 Native Ni-NTA pulldown

908 Cells were pelleted at 9727 x g for 1 min at 4°C. Pellets were lysed with native lysis buffer
909 (50 mM NaH_2PO_4, 300 mM NaCl, 0.2% NP-40, pH 8.0) complemented with 25 mM
910 Imidazole, protease (Roche, 04693116001) and phosphatase inhibitors (Roche,
911 4906845001), respectively. Lysed pellets were incubated on ice for 30 min. After incubation,
912 lysed pellets were centrifuged at 12000 x g for 15 min at 4°C and supernatant was collected
913 for total protein quantification. Ni-NTA spin columns (Qiagen, 31014) were used to purify
914 6HIS-tagged TAX1BP1 and its interacting proteins following provider instructions. Briefly,
915 Ni-NTA spin columns were first equilibrated using native lysis buffer with 25 mM Imidazole
916 and centrifuged for 2 min at 890 x g. After equilibration, 250 µg of total protein were loaded
917 on the columns and lysates were centrifuged at 270 x g for 10 min. Ni-NTA columns were
918 washed three times with lysis buffer containing 50 mM imidazole, centrifuged for 2 min at
919 890 x g. After washing, pulldown fractions were collected with elution buffer (50 mM
920 NaH_2PO_4, 300 mM NaCl, 0.2% NP-40, 500 mM Imidazole, pH 8.0) at 890 x g for 2 min
921 twice. Samples were sent directly in elution buffer for mass spectrometry analysis.

922 Ubiquitin pulldown

923 Cells were regularly washed with PBS before harvesting. After harvesting, cell pellets were
924 centrifuged at 9727 x g for 1 min at 4°C. Pellets were resuspended in RIPA buffer (50 mM
925 Tris/HCl, 150 mM NaCl, 1% NP-40, 0,5% deoxycholate, 0,2% SDS at pH 7.5) containing

926 phosphatase and protease inhibitors and left on ice. After 30 min, homogenates were
927 centrifuged at 18.000 x g for 15 min at 4°C and supernatant was recovered. Protein
928 concentration was measurement using the Pierce BCA assay kit (ThermoFischer). Ubiquitin
929 affinity beads (#UBA01B, Cytoskeleton) were used to pulldown ubiquitinated proteins. First,
930 both ubiquitin affinity beads and control beads (#CUB02B, Cytoskelton) were reconstituted
931 following manufacturer's instructions. For each pulldown reaction, 20 µl of ubiquitin or
932 control beads were aliquoted in a tube on ice and further washed twice with TBS-T.
933 Following bead wash, 200 µg of total protein were loaded on the beads. Pulldown reaction
934 tubes were filled with dilution buffer (50 mM Tris/HCl, 150 mM NaCl) containing protease
935 and phosphatase inhibitors to reach 1.5 ml of volume and were left in a rotating platform for
936 2 h at 4°C. After incubation, beads were collected and washed with dilution buffer. Three
937 washing steps were performed as follows: after buffer addition, tubes were allowed to rotate
938 for 5 min at 4°C, further pelleted at 5.000 x g for 1 minute at 4°C and supernatant was
939 removed. After the final wash, supernatant was completely removed with a Hamilton needle
940 and 50 µl of reducing buffer was added instead. Samples were boiled for 10 min at 95°C.
941 Bead pellets were further centrifuged at 5.000 x g for 1 minute at 4°C and supernatant was
942 collected. Samples were further analyzed via Western Blot.

943 Mass spectrometry

944 Eluates were mixed with 4x LDS sample buffer and proteins were separated by short SDS-
945 PAGE runs using NuPAGE NovexR Bis-Tris 4–12% Mini Gels (Invitrogen, NP0335BOX).
946 Protein bands were stained using QC Colloidal Coomassie Stain (Bio Rad Laboratories,
947 1610803) and whole sample lanes were excised. Gel pieces were further cut into small pieces
948 prior to in-gel digestion. Gel pieces were destained by incubation with 5 mM ABC in 50%

949 (v/v) ACN for 20 min three times and dehydrated using acetonitrile. Cysteine bonds were
950 reduced by incubation with 10 mM DTT for 45 min at 65°C before carbamidomethylation
951 by incubation with 55 mM iodoacetamide for 45 min at RT in the dark. Gel pieces were
952 washed two times and dehydrated as before, followed by digestion with trypsin overnight at
953 37°C. Peptides were extracted in three consecutive incubation steps with Extraction buffer A
954 (50% (v/v) ACN, 3% trifluoroacetic acid [TFA]), Extraction buffer B (80% (v/v) ACN, 0.5%
955 (v/v) TFA) and acetonitrile for 30 min each. Supernatants of each extraction were pooled,
956 and acetonitrile was evaporated by vacuum centrifugation. Peptides were purified using
957 StageTips [58]. Mass spectrometric analysis was performed using an Orbitrap Exploris 480
958 online (Thermo Fisher Scientific, Germany) coupled to an EASY nLC-1200 system (Thermo
959 Fisher Scientific, Germany). Peptides were separated on a 20 cm HPLC column with 75 µm
960 inner diameter (CoAnn Technologies, ICT36007508F-50) in-house packed with 1.9 µm
961 ReproSil-Pur C18 -AQ silica beads (Dr. Maisch HPLC GmbH, r119.aq.0001) and eluted by
962 solvent B in a 60 min linear gradient from 5–33% at a flow rate of 200 nL/min. Carry-over
963 was minimized by 30 min wash runs after each sample. Ionization was performed by ESI and
964 the mass spectrometer was operated in positive ion mode controlled by XCalibur (Thermo
965 Fisher Scientific). Acquisition of spectra was performed with a scan range of 350 – 950 m/z
966 and a resolution on the MS1 level of 60 000. MS2 scans were performed using DIA isolation
967 windows of 8 m/z with an overlap of 1 m/z (75 isolation windows), HCD collision energy of
968 30% and resolution of 15 000. The mass spectrometry proteomics data have been deposited
969 to the ProteomeXchange Consortium via the PRIDE partner repository [59] with the dataset
970 identifier PXD063982.

971

972 Mass spectrometry analysis

973 Raw files were processed using Spectronaut version 19 in directDIA+ mode using optimized
974 identification settings as described before [60]. Spectra were predicted using a Uniprot *Homo*
975 *sapiens* database (104 556 entries, downloaded on 2024/01/30). The data were exported using
976 the protein pivot report using PG.ProteinGroups as a unique protein ID and the PG.Quantity
977 as a quantification column. Data analysis was performed using Perseus version 2.0.5.0 [61],
978 Microsoft Excel and R. Proteins were annotated functionally and by compartment using Gene
979 Ontology Biological Processes and Gene Ontology Cellular Compartment databases (both
980 downloaded on 2024/10/29) as well as for mitochondrial sub-compartments using
981 MitoCarta3.0 (downloaded on 2021/02/24). To assess differences between WT and mutant
982 TAX1BP1, student's T-tests were performed on protein intensities normalized to the protein
983 quantities of the empty vector for both CCCP only and CCCP and BafA treated samples.
984 Significantly up- and downregulated proteins ($p<0.05$) were further analyzed for statistical
985 overrepresentation on GO biological processes using the panther database (pantherdb.org,
986 version 19.0) [23].

987 CellProfiler-based image analysis

988 The version 4.2.1 of the CellProfiler software was used [62]. All analyses rely on pooled
989 single cell values obtained from at least three independent biological replicates. In general,
990 individual cells were initially recognized with the nuclear staining and a cytoplasm area of
991 80-200 pixels (px) around the nucleus was further categorized as the cytoplasm, unless
992 otherwise noted. Areas of interest per cell correspond to the established cytoplasm without
993 the nucleus area.

994 For the analysis of mitochondrial clustering in WT-Parkin HeLa transfected with His-empty
995 or HIS-tagged TAX1BP1, mitochondrial material was recognized using SSBP1 signal as
996 primary object. SSBP1 objects were identified using a robust background two-class
997 thresholding method with lower and upper threshold bounds of 0.0-1.0, an adaptive window
998 of 50 and a size range of 6-500 px. Next, single SSBP1 objects that were in close contact
999 were merged (distance between objects=0 px). To account for only positively TAX1BP1
1000 transfected cells, TAX1BP1 was recognized as primary objects using a minimum cross
1001 entropy two-class thresholding method with a lower and upper threshold bounds of 0.0-1.0,
1002 an adaptive window of size 30 and a size range of 10-40 px. Only cells with positive
1003 TAX1BP1 signal (count TAX1BP1 objects>0) were taken into account for the TAX1BP1
1004 overexpressing (OE) condition.

1005 For the analysis of mitochondria clustering in 5KO HeLa co-expressing parkin as well as
1006 WT-, K549R and TAX1BP1ΔCC3, the analysis was performed similarly as previously
1007 described for the WT-Parkin HeLa with some variations. Mitochondrial material was
1008 recognized as SSBP1 signal using a roust background two-class thresholding method with
1009 lower and upper threshold bounds of 0.002-1.0, an adaptive window of size 50 and a size
1010 range of 4-500 px. TAX1BP1 was recognized as primary objects using a minimum cross-
1011 entropy two-class thresholding method with lower and upper threshold bounds of 0.0022-
1012 1.0, an adaptive window of size 80 and a size range of 6-40 px. Similarly, Parkin expression
1013 was monitored by recognizing parkin signal as primary object using a minimum cross-
1014 entropy two-class thresholding method with lower and upper threshold bounds of 0.0015-
1015 1.0, an adaptive window of size 50 and a size range of 10-40 px. Parkin objects were further
1016 merged if they were in close contact (object distance=0 px). Only cells with positive

1017 TAX1BP1 and parkin signal (mean object area > 0) were taken into account for this analysis.
1018 Values of total mean SSBP1 area and mitochondrial area or perimeter normalized by cell size
1019 (area or perimeter) are shown. For the analysis of TAX1BP1 distribution on SSBP1 clusters,
1020 only cells with a mean TAX1BP1 intensity of ≥10 aiu (arbitrary intensity units) were taken
1021 into account and the recognition method of TAX1BP1 and parkin signals was optimized. In
1022 this case, TAX1BP1 and parkin were recognized as primary objects using a robust
1023 background two-class thresholding method with lower and upper threshold bounds of
1024 0.0035-1.0 (for TAX1BP1) or 0.002-1.0 (for parkin) with a size range recognition of 3-40 px
1025 in both cases. Mitochondria were recognized using SSBP1 signal as described before for
1026 5KO HeLa. To measure the overlapping area between TAX1BP1-SSBP1 and parkin-SSBP1,
1027 total SSBP1 area was masked with TAX1BP1 or parkin merged objects and the percentage
1028 of SSBP1 overlapped by each protein was calculated (% SSBP1 recognized). Similarly,
1029 percentages of TAX1BP1 or parkin on mitochondria were calculated by considering which
1030 portion of the total TAX1BP1 or parkin area was engaged with mitochondrial material (%
1031 TAX1BP1 or parkin on SSBP1).

1032 For the analysis of size classification of TAX1BP1^{+} puncta and TAX1BP1-HSP60 material
1033 overlap in WT-Parkin (a) and 5KO-PRKN HeLa (b), cell area was recognized using a
1034 watershed-image method with nuclei as a reference point and TAX1BP1 or Parkin signal to
1035 identify cell contours (minimum cross entropy method, threshold bounds: 0.00001-1).
1036 TAX1BP1 puncta were recognized as primary objects using robust background method with
1037 lower and upper threshold bounds of 0.000001-1.0 in (a) and 0.0015-1.0 in (b), an adaptive
1038 window of size 15 and a size range of 4-40 px. In WT-Parkin Hela, only cells with TAX1BP1
1039 mean intensity of 0.004 aiu were considered. To optimize the recognition of individual

1040 puncta, clumped objects were distinguished by shape but dividing lines between clumped
1041 objects were intensity-based. TAX1BP1 objects were merged when in contact with each
1042 other (distance = 0 px), this step allowed to merge TAX1BP1 puncta that were in close
1043 contact with other TAX1BP1 puncta and were particularly difficult to recognize as single
1044 objects. Upon merging TAX1BP1 single objects, objects with an area form factor of 0.68-
1045 0.8 were kept (form factor=1 for a perfectly circular object). This step allowed to keep
1046 relatively circular-shaped objects (individual puncta) and discard merged objects that were
1047 the result of multiple TAX1BP1 puncta. Thus, not all TAX1BP1 puncta were taken into
1048 account for this analysis. After filtering, TAX1BP1 puncta were classified based on their
1049 size: enlarged puncta (area>150 px^2), intermediate puncta (area≤150 px^2) and small puncta
1050 (area<50 px^2). Mitochondrial material (HSP60) was recognized as primary object using a
1051 robust background method with lower and upper threshold bounds of 0.001-1 and a size range
1052 of 1-40 px in (a) and 0.0018-1.0 and a size range of 4-200 px in (b) and a size. HSP60 objects
1053 were used to mask enlarged, intermediate and small TAX1BP1 puncta. In WT-Parkin Hela,
1054 all TAX1BP1 puncta sizes were classified between HSP60-positive or HSP60-negative
1055 according to their overlap. Percentages of HSP60 puncta co-localizing with overall or
1056 enlarged TAX1BP1 puncta are shown as well as the corresponding HSP60 puncta area co-
1057 localizing with enlarged TAX1BP1 puncta. For each analyzed image of this analysis, output
1058 images were generated, showing the localization of the classified TAX1BP1 puncta, the cell
1059 limits. Colocalization analysis in 5KO-PRKN was performed using the
1060 MeasureColocalization module in CellProfiler, where Pearson's correlation coefficient of
1061 TAX1BP1 and HSP60 signals were computed per cell.

1062 Colocalization analysis of TAX1BP1-HSP60 and LC3B-HSP60 in 5KO-PRKN HeLa was
1063 performed similarly as described before with some variations. To ensure the analysis only
1064 included cells with similar TAX1BP1 expression, cells with a minimum mean integrated
1065 intensity of 7 aiu were considered. A TAX1BP1 background region was established to filter
1066 out cells with excessive TAX1BP1 levels (max. integrated intensity of 20 aiu overlapping
1067 nucleus). HSP60 objects were recognized as previously described. TAX1BP1 objects were
1068 recognized using robust background method with lower and upper threshold bounds of
1069 0.0022-1.0 and a size of 1-100 px. LC3B was recognized using a three-class Otsu method.
1070 Co-localization parameters were measured per each recognized cells for all three channels
1071 and Pearson's coefficient as well as thresholded Mander's coefficient were obtained.

1072 Statistics

1073 All data is derived from at least three independent biological replicates unless otherwise
1074 indicated. Statistical analysis and graph depiction of the data was performed using GraphPad
1075 Prism 8.0.2. Statistical significance was established at $p<0.05$ unless otherwise indicated.
1076 Significance was assessed by using a one-way ANOVA for multiple comparisons and
1077 subsequent Tukey's post-hoc test unless otherwise indicated. For the correlation analysis of
1078 TAX1BP1 binding to depolarized mitochondria, a Pearson correlation test was performed.
1079 For analysis in which only two conditions were compared, significance was assessed with an
1080 unpaired t-test analysis. The following significance indicators were used: ****: $p<0.001$,
1081 ***: $p<0.005$, **: $p<0.005$, *: $p<0.05$

1082

1083

1084 **Acknowledgements**

1085 PentaKO (5KO) HeLa cells were kindly provided by Dr. Chunxin (Black) Wang and Dr.
1086 Richard J. Youle, NINDS. This work was supported by the DFG Research Training Group
1087 2364 "MOMbrane", the Hertie Foundation and the German Center for Neurodegenerative
1088 Diseases. We would also like to acknowledge Prof. Dr. Tassula Proikas-Cezanne for valuable
1089 discussion and feedback. Lastly, we would also like to acknowledge Henrietta Lacks and her
1090 family.

1091

1092 **Conflict of interest**

1093 The authors declare no conflict of interest.

1094

1095 **Data availability**

1096 All mass spectrometry proteomics data have been deposited to the ProteomeXchange
1097 Consortium via the PRIDE partner repository and are openly available in
1098 http://www.ebi.ac.uk/pride with the dataset identifier PXD063982.

1099

1100 **References**

1101 [1] Narendra DP, Kane LA, Hauser DN, et al. p62/SQSTM1 is required for Parkin-
1102 induced mitochondrial clustering but not mitophagy; VDAC1 is dispensable for

1103 both. Autophagy 2010; 6(8):1090–106. doi: 10.4161/auto.6.8.13426

1104 [2] Geisler S, Holmström KM, Skujat D, et al. PINK1/Parkin-mediated mitophagy is
1105 dependent on VDAC1 and p62/SQSTM1. Nat Cell Biol 2010; 12(2):119–31. doi:
1106 10.1038/ncb2012

1107 [3] Matsuda N, Sato S, Shiba K, et al. PINK1 stabilized by mitochondrial depolarization
1108 recruits Parkin to damaged mitochondria and activates latent Parkin for mitophagy. J
1109 Cell Biol 2010; 189(2):211–21. doi: 10.1083/jcb.200910140

1110 [4] Narendra DP, Jin SM, Tanaka A, et al. PINK1 is selectively stabilized on impaired
1111 mitochondria to activate Parkin. PLoS Biol 2010; 8(1). doi:
1112 10.1371/journal.pbio.1000298

1113 [5] Kondapalli C, Kazlauskaite A, Zhang N, et al. PINK1 is activated by mitochondrial
1114 membrane potential depolarization and stimulates Parkin E3 ligase activity by
1115 phosphorylating Serine 65. Open Biol 2012; 2(MAY). doi: 10.1098/rsob.120080

1116 [6] Shiba-Fukushima K, Imai Y, Yoshida S, et al. PINK1-mediated phosphorylation of
1117 the Parkin ubiquitin-like domain primes mitochondrial translocation of Parkin and
1118 regulates mitophagy. Sci Rep 2012; 2:1–8. doi: 10.1038/srep01002

1119 [7] Koyano F, Okatsu K, Kosako H, et al. Ubiquitin is phosphorylated by PINK1 to
1120 activate parkin. Nature 2014; 510(7503):162–6. doi: 10.1038/nature13392

1121 [8] Ordureau A, Heo JM, Duda DM, et al. Defining roles of PARKIN and ubiquitin
1122 phosphorylation by PINK1 in mitochondrial quality control using a ubiquitin
1123 replacement strategy. Proc Natl Acad Sci U S A 2015; 112(21):6637–42. doi:
1124 10.1073/pnas.1506593112

1125 [9] Lechado-Terradas A, Schepers S, Zittlau KI, et al. Parkin-dependent mitophagy
1126 occurs via proteasome-dependent steps sequentially targeting separate mitochondrial
1127 sub-compartments for autophagy. Autophagy Reports 2022; 1(1):576–602. doi:
1128 10.1080/27694127.2022.2143214

1129 [10] Heo JM, Ordureau A, Paulo JA, et al. The PINK1-PARKIN Mitochondrial
1130 Ubiquitylation Pathway Drives a Program of OPTN/NDP52 Recruitment and TBK1
1131 Activation to Promote Mitophagy. Mol Cell 2015; 60(1):7–20. doi:
1132 10.1016/j.molcel.2015.08.016

1133 [11] Lazarou M, Sliter DA, Kane LA, et al. The ubiquitin kinase PINK1 recruits
1134 autophagy receptors to induce mitophagy. Nature 2015; 524(7565):309–14. doi:
1135 10.1038/nature14893

1136 [12] Richter B, Sliter DA, Herhaus L, et al. Phosphorylation of OPTN by TBK1 enhances
1137 its binding to Ub chains and promotes selective autophagy of damaged
1138 mitochondria. Proc Natl Acad Sci U S A 2016; 113(15):4039–44. doi:
1139 10.1073/pnas.1523926113

1140 [13] Yamano K, Kikuchi R, Kojima W, et al. Critical role of mitochondrial ubiquitination
1141 and the OPTN ATG9A axis in mitophagy. J Cell Biol 2020; 219(9). doi:
1142 10.1083/jcb.202001120

1143 [14] Nguyen TN, Sawa-makarska J, Khuu G, et al. Unconventional initiation of
1144 PINK1/Parkin mitophagy by Optineurin. Mol Cell 2023; 83(10):1693–709. doi:
1145 10.1016/j.molcel.2023.04.021

1146 [15] Turco E, Savova A, Gere F, et al. Reconstitution defines the roles of p62, NBR1 and

1147 TAX1BP1 in ubiquitin condensate formation and autophagy initiation. Nat Commun
1148 2021; 12(1):1–16. doi: 10.1038/s41467-021-25572-w

1149 [16] Yamano K, Sawada M, Kikuchi R, et al. Optineurin provides a mitophagy contact
1150 site for TBK1 activation. EMBO J 2024; 43(5):754–79. doi: 10.1038/s44318-024-
1151 00036-1

1152 [17] Zittlau KI, Lechado-Terradas A, Nalpas N, et al. Temporal Analysis of Protein
1153 Ubiquitylation and Phosphorylation During Parkin-Dependent Mitophagy. Mol Cell
1154 Proteomics 2022; 21(2):100191. doi: 10.1016/j.mcpro.2021.100191

1155 [18] Rose CM, Isasa M, Ordureau A, et al. Highly Multiplexed Quantitative Mass
1156 Spectrometry Analysis of Ubiquitylomes. Cell Syst 2016; 3(4):395-403.e4. doi:
1157 10.1016/j.cels.2016.08.009

1158 [19] Narendra DP, Youle RJ. The role of PINK1–Parkin in mitochondrial quality control.
1159 Nat Cell Biol 2024; 26(October). doi: 10.1038/s41556-024-01513-9

1160 [20] Adriaenssens E, Ferrari L, Martens S. Orchestration of selective autophagy by cargo
1161 receptors. Curr Biol 2022; 32(24):R1357–71. doi: 10.1016/j.cub.2022.11.002

1162 [21] Sharma K, Kishore A, Lechado-Terradas A, et al. A Novel PINK1 p.F385S Loss-of-
1163 Function Mutation in an Indian Family with Parkinson's Disease. Mov Disord 2024;
1164 39(7):1217–25. doi: 10.1002/mds.29792

1165 [22] Zhao YG, Codogno P, Zhang H. Machinery, regulation and pathophysiological
1166 implications of autophagosome maturation. Nat Rev Mol Cell Biol 2021;
1167 22(11):733–50. doi: 10.1038/s41580-021-00392-4

1168 [23] Mi H, Muruganujan A, Csagrande JT, et al. Large-scale gene function analysis with

1169 PANTHER Classification System. Nat Protoc 2013; 8(8):1551–66. doi:
1170 10.1038/nprot.2013.092

1171 [24] Wang J, Davis S, Zhu M, et al. Autophagosome formation: Where the secretory and
1172 autophagy pathways meet. Autophagy 2017; 13(5):973–4. doi:
1173 10.1080/15548627.2017.1287657

1174 [25] Bhattacharjee S, Lee Y, Zhu B, et al. Epsins in vascular development, function and
1175 disease. Cell Mol Life Sci 2021; 78(3):833–42. doi: 10.1007/s00018-020-03642-4

1176 [26] Hida Y, Ohtsuka T. CAST and ELKS proteins: Structural and functional
1177 determinants of the presynaptic active zone. J Biochem 2010; 148(2):131–7. doi:
1178 10.1093/jb/mvq065

1179 [27] Ramella M, Ribolla LM, de Curtis I. Liquid–Liquid Phase Separation at the Plasma
1180 Membrane–Cytosol Interface: Common Players in Adhesion, Motility, and Synaptic
1181 Function. J Mol Biol 2022; 434(1):167228. doi: 10.1016/j.jmb.2021.167228

1182 [28] Jackson TR, Brown FD, Nie Z, et al. ACAPs are arf6 GTPase-activating proteins
1183 that function in the cell periphery. J Cell Biol 2000; 151(3):627–38. doi:
1184 10.1083/jcb.151.3.627

1185 [29] Yamano K, Fogel AI, Wang C, et al. Mitochondrial Rab GAPs govern
1186 autophagosome biogenesis during mitophagy. Elife 2014; 3:1–24. doi:
1187 10.7554/elife.01612

1188 [30] Yamano K, Wang C, Sarraf SA, et al. Endosomal Rab cycles regulate Parkin-
1189 mediated mitophagy. 2018; :1–32.

1190 [31] Bakula D, Müller AJ, Zuleger T, et al. WIPI3 and WIPI4 β-propellers are scaffolds

1191 for LKB1-AMPK-TSC signalling circuits in the control of autophagy. Nat Commun
1192 2017; 8(May). doi: 10.1038/ncomms15637

1193 [32] Ji C, Zhao H, Chen D, et al. β-propeller proteins WDR45 and WDR45B regulate
1194 autophagosome maturation into autolysosomes in neural cells. Curr Biol 2021;
1195 31(8):1666-1677.e6. doi: 10.1016/j.cub.2021.01.081

1196 [33] Dikic I, Elazar Z. Mechanism and medical implications of mammalian autophagy.
1197 Nat Rev Mol Cell Biol 2018; 19(6):349–64. doi: 10.1038/s41580-018-0003-4

1198 [34] Lechado-Terradas A, Zittlau KI, Macek B, et al. Regulation of mitochondrial cargo-
1199 selective autophagy by posttranslational modifications. J Biol Chem 2021;
1200 297(5):101339. doi: 10.1016/j.jbc.2021.101339

1201 [35] Sarraf SA, Raman M, Guarani-Pereira V, et al. Landscape of the PARKIN-
1202 dependent ubiquitylome in response to mitochondrial depolarization. Nature 2013;
1203 496(7445):372–6. doi: 10.1038/nature12043

1204 [36] Jumper J, Evans R, Pritzel A, et al. Highly accurate protein structure prediction with
1205 AlphaFold. Nature 2021; 596(7873):583–9. doi: 10.1038/s41586-021-03819-2

1206 [37] Ling L, Goeddel D V. T6BP , a TRAF6-interacting protein involved in IL-1
1207 signaling. 2000; :2–7.

1208 [38] Johansen T, Lamark T. Selective autophagy mediated by autophagic adapter
1209 proteins. Autophagy 2011; 7(3):279–96. doi: 10.4161/auto.7.3.14487

1210 [39] Kataura T, Otten EG, Rabanal-Ruiz Y, et al. NDP52 acts as a redox sensor in
1211 PINK1/Parkin-mediated mitophagy. EMBO J 2023; 42(5):1–16. doi:
1212 10.15252/embj.2022111372

1213 [40] Manders L, Heyninck T, Imberechts D, et al. VPS35 mutation inhibits
1214 PINK1/parkin-mediated mitophagy via increased LRRK2 kinase activity. Brain
1215 2025; (October):1–18. doi: 10.1093/brain/awaf414

1216 [41] Mauthe M, Orhon I, Rocchi C, et al. Chloroquine inhibits autophagic flux by
1217 decreasing autophagosome-lysosome fusion. Autophagy 2018; 14(8):1435–55. doi:
1218 10.1080/15548627.2018.1474314

1219 [42] Tumbarello DA, Waxse BJ, Arden SD, et al. Autophagy receptors link myosin VI to
1220 autophagosomes to mediate Tom1-dependent autophagosome maturation and fusion
1221 with the lysosome. Nat Cell Biol 2012; 14(10):1024–35. doi: 10.1038/ncb2589

1222 [43] der Beek J van, de Heus C, Sanza P, et al. Loss of the HOPS complex disrupts early-
1223 to-late endosome transition, impairs endosomal recycling and induces accumulation
1224 of amphisomes. Mol Biol Cell 2024; 35(3):1–24. doi: 10.1091/MBC.E23-08-0328

1225 [44] Zellner S, Schifferer M, Behrends C. Systematically defining selective autophagy
1226 receptor-specific cargo using autophagosome content profiling. Mol Cell 2021;
1227 81(6):1337-1354.e8. doi: 10.1016/j.molcel.2021.01.009

1228 [45] Heo JM, Harper NJ, Paulo JA, et al. Integrated proteogenetic analysis reveals the
1229 landscape of a mitochondrial-autophagosome synapse during PARK2-dependent
1230 mitophagy. Sci Adv 2019; 5(11). doi: 10.1126/sciadv.aay4624

1231 [46] Morinaka K, Koyama S, Nakashima S, et al. Epsin binds to the EH domain of POB1
1232 and regulates receptor-mediated endocytosis. Oncogene 1999; 18(43):5915–22. doi:
1233 10.1038/sj.onc.1202974

1234 [47] Stankewich MC, Stabach PR, Morrow JS. Human Sec31B: A family of new

1235 mammalian orthologues of yeast Sec31p that associate with the COPII coat. J Cell
1236 Sci 2006; 119(5):958–69. doi: 10.1242/jcs.02751

1237 [48] Mancias JD, Goldberg J. Structural basis of cargo membrane protein discrimination
1238 by the human COPII coat machinery. EMBO J 2008; 27(21):2918–28. doi:
1239 10.1038/emboj.2008.208

1240 [49] Hurley JH, Young LN. Mechanisms of autophagy initiation. Annu Rev Biochem
1241 2017; 86:225–44. doi: 10.1146/annurev-biochem-061516-044820

1242 [50] Davis S, Wang J, Zhu M, et al. Sec24 phosphorylation regulates autophagosome
1243 abundance during nutrient deprivation. Elife 2016; 5(NOVEMBER2016):1–22. doi:
1244 10.7554/eLife.21167

1245 [51] Nie J, Ma S, Wu L, et al. SEC31a-ATG9a Interaction Mediates the Recruitment of
1246 COPII Vesicles for Autophagosome Formation. Adv Sci 2024; 2405127:1–15. doi:
1247 10.1002/advs.202405127

1248 [52] Gyurkovska V, Murtazina R, Zhao SF, et al. Dual function of Rab1A in secretion
1249 and autophagy: hypervariable domain dependence. Life Sci Alliance 2023; 6(5):1–
1250 16. doi: 10.26508/lsa.202201810

1251 [53] Haga K, Fukuda M. Comprehensive knockout analysis of the RAB family small
1252 GTPases reveals an overlapping role of RAB2 and RAB14 in autophagosome
1253 maturation. Autophagy 2024; 21(1):21–36. doi: 10.1080/15548627.2024.2374699

1254 [54] Wartosch L, Günesdogan U, Graham SC, et al. Recruitment of VPS33A to HOPS by
1255 VPS16 Is Required for Lysosome Fusion with Endosomes and Autophagosomes.
1256 Traffic 2015; 16(7):727–42. doi: 10.1111/tra.12283

1257 [55] Geisler S, Jäger L, Golombek S, et al. Ubiquitin-specific protease USP36
1258 knockdown impairs Parkin-dependent mitophagy via downregulation of Beclin-1-
1259 associated autophagy-related ATG14L. Exp Cell Res 2019; 384(2):111641. doi:
1260 10.1016/j.yexcr.2019.111641

1261 [56] Geisler S, Vollmer S, Golombek S, et al. The ubiquitin-conjugating enzymes
1262 UBE2N, UBE2L3 and UBE2D2/3 are essential for Parkin-dependent mitophagy. J
1263 Cell Sci 2014; 127(15):3280–93. doi: 10.1242/jcs.146035

1264 [57] Alberio T, Pieroni L, Ronci M, et al. Toward the Standardization of Mitochondrial
1265 Proteomics: The Italian Mitochondrial Human Proteome Project Initiative. J
1266 Proteome Res 2017; 16(12):4319–29. doi: 10.1021/acs.jproteome.7b00350

1267 [58] Rappsilber J, Mann M, Ishihama Y. Protocol for micro-purification, enrichment, pre-
1268 fractionation and storage of peptides for proteomics using StageTips. Nat Protoc
1269 2007; 2(8):1896–906. doi: 10.1038/nprot.2007.261

1270 [59] Perez-Riverol Y, Bandla C, Kundu DJ, et al. The PRIDE database at 20 years: 2025
1271 update. Nucleic Acids Res 2025; 53(D1):D543–53. doi: 10.1093/nar/gkae1011

1272 [60] Bruderer R, Bernhardt OM, Gandhi T, et al. Optimization of experimental
1273 parameters in data-independent mass spectrometry significantly increases depth and
1274 reproducibility of results. Mol Cell Proteomics 2017; 16(12):2296–309. doi:
1275 10.1074/mcp.RA117.000314

1276 [61] Tyanova S, Temu T, Sinitcyn P, et al. The Perseus computational platform for
1277 comprehensive analysis of (prote)omics data. Nat Methods 2016; 13(9):731–40. doi:
1278 10.1038/nmeth.3901

1279 [62] Stirling DR, Swain-Bowden MJ, Lucas AM, et al. CellProfiler 4: improvements in
1280 speed, utility and usability. BMC Bioinformatics 2021; 22(1):1–11. doi:
1281 10.1186/s12859-021-04344-9

1282 [63] Meng EC, Goddard TD, Pettersen EF, et al. UCSF ChimeraX: Tools for structure
1283 building and analysis. Protein Sci 2023; 32(11):1–13. doi: 10.1002/pro.4792

1284

1285

1286

1287

1288

1289

1290

1291

1292

1293

1294

1295

1296

1297

1298

1299 **Figure legends**

1300 **Figure 1: Ubiquitination of TAX1BP1 upon CCCP-induced mitophagy in HeLa cells**
1301 **stably expressing WT- or C431A-Parkin.** (**A**) Schematic representation of TAX1BP1
1302 domain structure. Identified ubiquitinated lysine residues from the ubiquitylome mass-
1303 spectrometry screen are indicated in red. (**B**) Normalized Gly-Gly peptide signals of the
1304 identified ubiquitinated residues in both WT- and C431A-parkin HeLa cell lines during
1305 mitophagy induction at the indicated time points. (**C**) Western blot detection of the indicated
1306 proteins in whole cell lysates from HeLa cells stably expressing WT- or catalytically inactive
1307 C431A-parkin treated with CCCP for the indicated times. TAX1BP1 band shift peaking at 4
1308 h confirms ubiquitination. (**D**) Western blots showing protein signals of 5% of input or 10%
1309 of eluted pulldown samples performed in WT-Parkin Hela depolarized with CCCP for 4 h or
1310 under control conditions (DMSO). Pulldown samples are shown for three independent
1311 replicate experiments (Rep).

1312

1313 **Figure 2: TAX1BP1 translocation to mitochondria during CCCP-induced mitophagy.**
1314 (**A**) Representative immunofluorescence images showing endogenous TAX1BP1 (yellow),
1315 and the inner mitochondrial marker SSBP1 (cyan) at basal levels or after mitophagy induction
1316 (10 µM CCCP, 2h). Scale bars: 5 µm (**B**) Subcellular fractionation of WT-Parkin HeLa cells
1317 under basal conditions or after short depolarization, where translocation of parkin and
1318 ubiquitinated TAX1BP1 to mitochondria can be observed. WCL: whole cell lysate, F1:
1319 fraction 1 corresponds to the supernatant recovered after the first centrifugation series, F2:
1320 fraction 2 corresponds to the supernatant recovered after the second centrifugation step in

1321 which the crude mitochondria pellet were obtained, CM: crude mitochondria fraction, MMF:
1322 membrane enriched fraction, MTF: mitochondrial enriched fraction.

1323

1324 **Figure 3: Over-expression of TAX1BP1ΔCC3 leads to changes in its ubiquitination**
1325 **pattern and reduces clearance of ubiquitinated TOM20**. (**A**) Schematic representation of
1326 the HIS-tagged TAX1BP1 constructs harboring residue-specific or deletion mutations at the
1327 CC3 domain. H: 6xHis-tag. (**B**) Mitophagy time course in 5KO-HeLa cells transiently
1328 expressing WT, TAX1BP1^{K549R} and TAX1BP1ΔCC3 with or without Flag-tagged WT-
1329 Parkin co-transfection. Ø: empty control plasmids. Color-coded legends are shown for each
1330 transfection condition. (**C**) Relative levels of ubiquitinated (Ub-) TAX1BP1 after the
1331 indicated CCCP treatments. Quantification corresponds to the Ub_n-TAX1BP1 smear
1332 indicated in panel (B). (**D**) Ubiquitin pulldown western blots showing protein signals of 5%
1333 of input or 10% of eluted samples performed in 5KO-PRKN HeLa depolarized for 4 h of
1334 CCCP compared to control conditions (DMSO). Red and blue arrowheads indicate presence
1335 or absence of poly-ubiquitinated TAX1BP1 bands, respectively. (**E**) Quantification of Ub-
1336 TAX1BP1 bands obtained in Ubiquitin pulldown shown in (D, lower panel). Ubiquitination
1337 levels were normalized to TAX1BP1 input signal for each transfection condition. Further,
1338 normalization to control beads and to DMSO control was performed. For this comparison,
1339 unpaired t-test was used to assess significance. (**F-I**) Relative protein levels of the following
1340 mitochondrial markers: VDAC (F), TOM20 (G), CS (H) and COX4 (I). Quantifications
1341 correspond to protein levels in 5KO Hela shown in (B). (**J**) Relative levels of ubiquitinated
1342 (Ub-) TOM20 after the indicated CCCP treatment shown in (B). All protein quantifications
1343 are derived from at least three independent experiments. Protein signal ratios in (F-I) were

1344 obtained after normalization of protein signal with loading control (vinculin) and subsequent
1345 normalization with protein values at basal level. Ubiquitination levels shown in panels (C)
1346 and (J) were normalized to loading and to TOM20 or TAX1BP1 levels, respectively. Ratios
1347 relative to empty transfection control are shown for TOM20 while for Ub-TAX1BP1, ratios
1348 are relative to Ub-TAX1BP1-WT levels after 2 h CCCP. One-way ANOVA was used to
1349 assess significance unless otherwise specified. Bars: Mean ± SEM.

1350

1351 **Figure 4: Single cell analysis of TAX1BP1 translocation to mitochondria after CCCP-**
1352 **mediated depolarization.** (**A**) Representative immunofluorescence images showing
1353 TAX1BP1 (yellow), parkin (magenta) and SSBP1 (cyan) after mitochondria depolarization
1354 in 5KO HeLa cells transiently co-expressing Parkin and TAX1BP1. Solid arrowheads
1355 indicate TAX1BP1 structures co-localizing with mitochondrial material. Arrows indicate
1356 TAX1BP1 structures not engaged with mitochondrial material. ROI 1 represents > 50 % of
1357 cell population while ROI 2 represents < 50% of cases. Scale bars: 10 µm. Zoom insets for
1358 WT (i), TAX1BP1^{K549R} (ii), TAX1BPΔCC3 (iii and iv) are shown below. (**B**) Mean
1359 mitochondrial size of SSBP1 foci after 4h CCCP. (**C-D**) Normalized SSBP1 (C) area or (D)
1360 perimeter per cell. (**E**) Correlation analysis of the percentage of mitochondrial area
1361 recognized by TAX1BP1 (X axis) in relation to the percentage of total TAX1BP1 found on
1362 mitochondria (Y axis). Significance p-values are indicated in the graph for the each
1363 TAX1BP1 construct. (**F**) Left panel: quantitative analysis of WT, TAX1BP1^{K549R} or
1364 TAX1BP1ΔCC3 localization after mitochondria depolarization in 5KO-PRKN cells after
1365 mitophagy induction (4h CCCP). TAX1BP1 localization is classified between cells where
1366 COX4 clumps are fully recognized by TAX1BP1 (complete apposition) and cells where

1367 COX4 clumps recognition is limited (localized apposition). Bars: mean ± SEM. Right panel:
1368 representative immunofluorescence images stained for TAX1BP1 (yellow) and COX4
1369 (magenta) are shown for each category represented in graph.
1370
1371 **Figure 5: Autophagy flux blockage effects in 5KO-PRKN HeLa cells.** (**A-B**)
1372 Representative immunofluorescence images of 5KO-PRKN HeLa cells showing TAX1BP1
1373 (yellow), parkin (magenta) and SSBP1 (cyan) after mitochondria depolarization only (A) or
1374 with Bafilomycin A (BafA) (B). In (A), the cell contour of cells lacking SSBP1 is
1375 highlighted. In (B), zoom insets are shown for WT (i), TAX1BP1^{K549R} (ii) and
1376 TAX1BPΔCC3 (iii), where solid arrowheads indicate enlarged TAX1BP1/SSBP1-positive
1377 puncta and thin arrowheads indicate small TAX1BP1/SSBP1-positive puncta**.** (**C-D**) Eye-
1378 based quantification of (C) cells with remaining SSBP1 material after extended
1379 depolarization (16 h CCCP) and (D) cells harboring enlarged or small TAX1BP1 puncta
1380 positive for SSBP1 (16 h CCCP + BafA). (**E**) Changes in TAX1BP1 ubiquitination after 16
1381 h of CCCP treatment combined with BafA. **(F)** Mean TAX1BP1 puncta size after autophagy
1382 blockage with BafA combined with CCCP or Oligomycin and Antimycin A (OA) treatment
1383 for 16 h. **(G)** Pearson correlation indexes for TAX1BP1 and HSP60 signals after CCCP and
1384 OA treatment combined with BafA. In panels (E) and (G), data of individual cells is
1385 represented by single dots. All data come from at least three independent experiments. **(H)**
1386 Percentages of cells showing at least 25% of TAX1BP1 enlarged puncta after the indicated
1387 treatments. Bars: Mean ± SEM. Scale bars: 10 µm. KR: K549R, ΔCC: ΔCC3.
1388

1389 **Figure 6: Characterization of enlarged TAX1BP1^{+} vesicles carrying mitochondrial**
1390 **material upon autophagy flux inhibition in 5KO-PARK.** (**A**) Representative images of
1391 5KO-PRKN HeLa cells showing enlarged TAX1BP1^{+} HSP60^{+} structures (magenta and cyan,
1392 respectively) positive for the autophagosome marker LC3B (yellow) after mitochondria
1393 depolarization and BafA for 16 h. Scale bars: 5 µm. (**B**) Z-stack projection of enlarged
1394 vesicles identified in (A) for WT, TAX1BP1^{K549R} and TAX1BP1ΔCC3. Thick arrowheads
1395 indicate LC3B^{+} TAX1BP1^{+} cup-shaped structures in each Z-plane. Thickness slice: 0.6 µm.
1396 (**C-E**) Representative images showing enlarged TAX1BP1^{+} HSP60^{+} structures positive for
1397 RAB7 (C), VPS35 (D) and CD63 (E). Zoom insets are shown for WT (i), TAX1BP1^{K549R} (ii)
1398 and TAX1BPΔCC3 (iii) for all markers. Scale bars: 5 µm.
1399
1400 **Figure 7: Characterization of small TAX1BP1^{+} vesicles carrying matrix mitochondrial**
1401 **material upon autophagy flux inhibition in 5KO-PARK.** (**A-D**) Representative images of
1402 5KO-PRKN HeLa cells showing small TAX1BP1/HSP60-positive structures (magenta,
1403 cyan) positive for the indicated markers (yellow): LC3B (A), RAB7 (B), VPS35 (C) and
1404 CD63 (D). Zoom insets are shown for WT (i), TAX1BP1^{K549R} (ii) and TAX1BPΔCC3 (iii)
1405 for all markers. Scale bars: 5 µm.
1406
1407 **Figure 8: Characterization of TAX1BP1^{+} structures identified in WT-Parkin Hela cells**
1408 **upon autophagy flux inhibition and extended depolarization.** (**A**) Representative images
1409 upon siRNA mediated knock-down of TAX1BP1 in WT-Parkin HeLa cells showing
1410 TAX1BP1^{+} structures (magenta) carrying mitochondrial material (HSP60, cyan). Scale bars:
1411 10 µm. Zoom insets are shown for the indicated conditions (right side, i-v). Lower panel of

1412 western blot insets illustrates silencing and re-transfection efficiency (n=2). (**B-G**)
1413 CellProfiler based analysis of TAX1BP1 puncta size or HSP60 material colocalizing with
1414 TAX1BP1 puncta in WT-Parkin HeLa cells after siRNA mediated TAX1BP1 knockdown
1415 and TAX1BP1 re-transfection upon CCCP and BafA treatment. (B) Mean TAX1BP1^{+} puncta
1416 size. (C) Percentage of intracellular enlarged TAX1BP1^{+} puncta per cell. (D) Percentage of
1417 total cells harboring enlarged TAX1BP1^{+} puncta. (E) Percentage of total HSP60 foci
1418 colocalizing with TAX1BP1. (F) Percentage of total HSP60 foci colocalizing with enlarged
1419 TAX1BP1^{+} puncta. (G) Mean HSP60 foci area colocalizing with enlarged TAX1BP1^{+}
1420 structures.
1421
1422 **Figure 9: Co-localization analysis of TAX1BP1 and LC3B on depolarized mitochondria**
1423 **upon overexpression of WT, TAX1BP1^{K549R} or TAX1BP1ΔCC3.** Depolarization was
1424 performed for 4 hours with CCCP or OA, as indicated. (**A)** Representative images showing
1425 TAX1BP1 (yellow), LC3B (magenta) and HSP60 (cyan) after 4 h of depolarization. Scale
1426 bars: 8 µm. (**B-E**) Colocalization analysis of TAX1BP1-HSP60 (B-C) and LC3B-HSP60 (D-
1427 E), represented with thresholded Manders coefficient or Pearson's correlation coefficient for
1428 the respective treatments and TAX1BP1 transfection, as indicated. (**F**) Mean LC3B intensity
1429 observed upon the indicated treatments and TAX1BP1 transfection. i.u: intensity units. (**G**)
1430 LC3B area relative to total cell area. In all panels, data of individual cells is represented by
1431 single dots. All data come from at least three independent experiments. KR: K549R, ΔCC:
1432 ΔCC3.
1433

1434 **Figure 10: Mass spectrometry analysis of TAX1BP1 native pulldown indicates defects**
1435 **in protein trafficking processes in TAX1BP1ΔCC3.** (**A**) Statistical analysis of
1436 TAX1BP1ΔCC3 vs. WT TAX1BP1 pulldowns represented by the $\log_{10}$ p-value plotted
1437 against student's T-test difference. Significance lines represent $p \leq 0.05$ and $p \leq 0.1$, as
1438 indicated. Proteins are grouped according to the following GO-Terms: vesicle-mediated
1439 transport in orange (GO:0016192), membrane organization in brown (GO:0061024) and
1440 mitophagy in red (GO:1903146; GO:1901524; GO:1905089; GO:1905091); mitochondria
1441 localization in lilac (based on UniProt annotation) or if they are associated with
1442 PINK1/parkin mitophagy in grey (based on literature). Proteins related to the GO-Term
1443 vesicle-mediated transport (GO:0016192) are classified according to their functionality
1444 (based on UniProt and literature); between endosome budding from Golgi (light green) or
1445 COPII vesicle related (dark green). (**B**) Overrepresentation analysis of biological processes
1446 for significantly regulated proteins by Fisher exact testing.

1447

1448 **Figure 11: Structural visualization of TAX1BP1 using the predicted Alphafold**
1449 **structure.** (**A**) Domain organization of the coiled-coil domains of TAX1BP1 according to
1450 Alphafold (top panel). Predicted Alphafold structure of TAX1BP1 with the indicated per-
1451 residue model confidence scores (pLDDT). In the zoom panel, identified lysines in the mass-
1452 spectrometry screen are highlighted in green. Highlighted in magenta are the remaining
1453 lysines of the CC3, which were not identified via MS. (**B**) TAX1BP1, structure in
1454 combination with a ubiquitin molecule at its ubiquitin-binding domain (UBD). Zoom panel
1455 shows lysines of CC3 (residue surface) in close proximity to the UBD. Highlighted lysines

1456 of CC3 are shown in green, if they were identified in the mass-spectrometry screen. The rest
1457 of lysines from CC3 are shown in magenta. Images created with ChimeraX [63].
1458
1459 **Figure 12: Graphical summary highlighting how reduced ubiquitination on TAX1BP1**
1460 **can influence the degradative pathway responsible for eliminating defective**
1461 **mitochondria in a PINK1/parkin context.** (**A**) Upon PINK1/parkin activation, TAX1BP1
1462 is ubiquitinated at the CC3 domain and translocates to mitochondria. Recognition of
1463 ubiquitinated mitochondria via TAX1BP1 promotes autophagosomal delivery. Simple
1464 autophagosomal-dependent degradation occurs after successful engulfment of defective
1465 mitochondria, autophagosome closure and autophagosome maturation, fostering the
1466 degradation of mitochondria. (**B**) Reduced TAX1BP1 ubiquitination or lack of the
1467 ubiquitinatable CC3 domain of TAX1BP1 in a context of PINK1/parkin mitophagy follows
1468 a slightly different behavior. Here, while TAX1BP1 is able to recognize ubiquitinated
1469 mitochondria, its translocation to mitochondria is hampered when compared to WT/normal
1470 conditions. This recognition is able to induce the formation of autophagosomes around
1471 defective mitochondria in this case, albeit at lower level. Recruitment of LC3-positive
1472 vesicles occurs in a more localized manner, which deviates mitophagy dynamics from this
1473 point on. Although this pathway leads to successful degradation of defective mitochondria,
1474 in this case the prevailed degradative pathway is more dependent on the endolysosomal
1475 network rather than on the classical autophagy machinery.

Figure 1

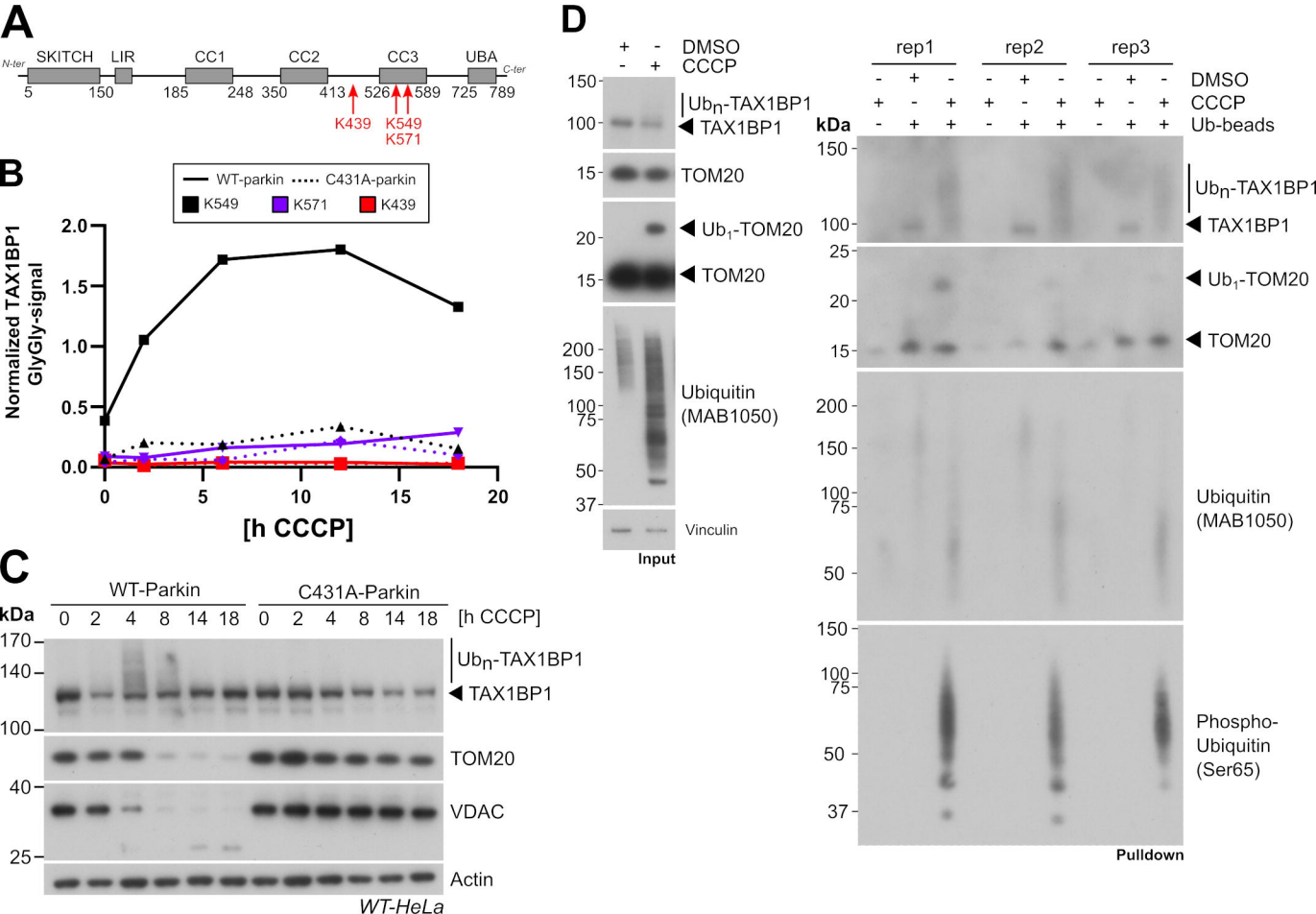
A
N-ter
SKITCH
LIR
CC1
CC2
CC3
UBA
C-ter
5
150
185
248
350
413
526
589
725
789
K439
K549
K571
B
WT-parkin
C431A-parkin
K549
K571
K439
Normalized TAX1BP1 GlyGly-signal
2.0
1.5
1.0
0.5
0.0
0
5
10
15
20
[h CCCP]
C
WT-Parkin
C431A-Parkin
kDa
0 2 4 8 14 18
0 2 4 8 14 18
[h CCCP]
170
140
100
40
25
Ubn-TAX1BP1
TAX1BP1
TOM20
VDAC
Actin
WT-HeLa
D
DMSO
CCCP
150
100
15
20
15
200
150
100
75
50
37
Ubn-TAX1BP1
TAX1BP1
TOM20
Ub1-TOM20
TOM20
Ubiquitin
(MAB1050)
Vinculin
Input
rep1
rep2
rep3
DMSO
CCCP
Ub-beads
kDa
150
100
25
20
15
200
150
100
75
50
150
100
75
50
37
Ubn-TAX1BP1
TAX1BP1
Ub1-TOM20
TOM20
Ubiquitin
(MAB1050)
Phospho-
Ubiquitin
(Ser65)
Pulldown

Figure 2

A

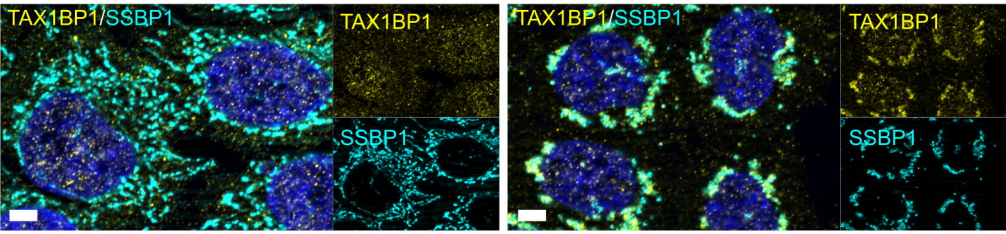
DMSO
CCCP
TAX1BP1/SSBP1
TAX1BP1
SSBP1
TAX1BP1/SSBP1
TAX1BP1
SSBP1

B

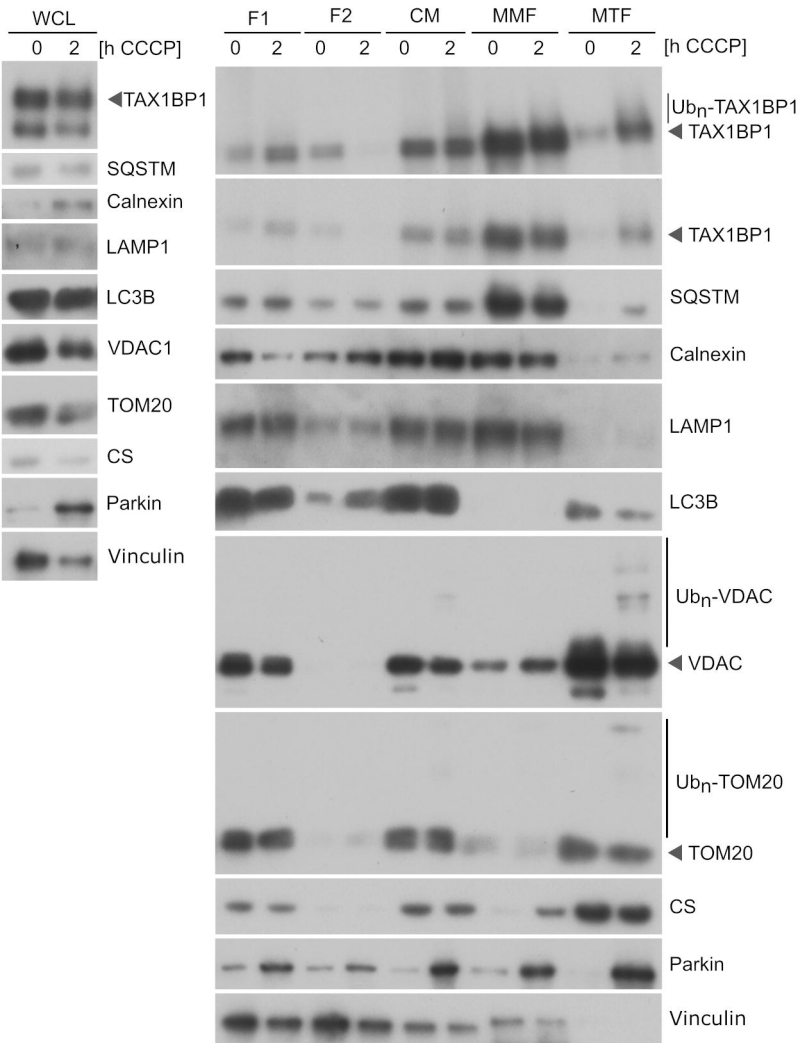
WCL
0 2 [h CCCP]
TAX1BP1
SQSTM
Calnexin
LAMP1
LC3B
VDAC1
TOM20
CS
Parkin
Vinculin
F1 F2 CM MMF MTF
0 2 0 2 0 2 0 2 0 2 [h CCCP]
Ubn-TAX1BP1
TAX1BP1
TAX1BP1
SQSTM
Calnexin
LAMP1
LC3B
Ubn-VDAC
VDAC
Ubn-TOM20
TOM20
CS
Parkin
Vinculin

Figure 3

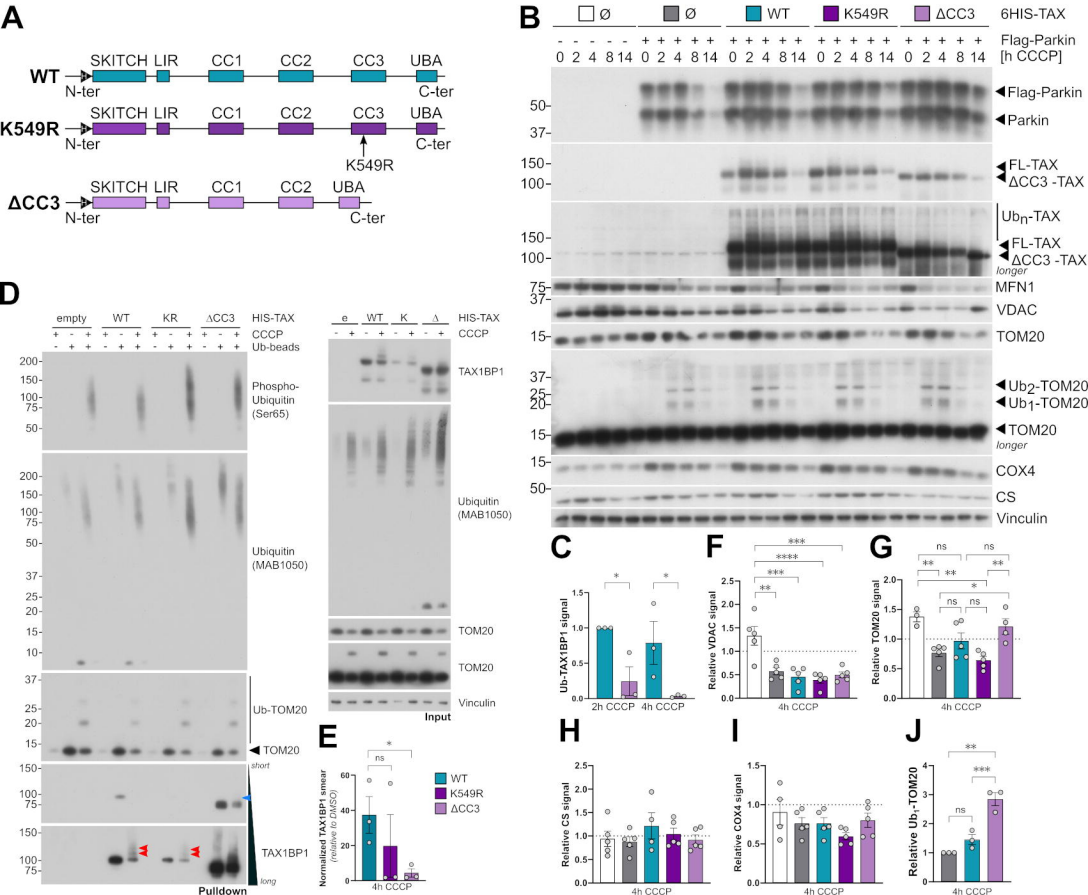

A
WT
SKITCH LIR CC1 CC2 CC3 UBA
N-ter
C-ter
K549R
SKITCH LIR CC1 CC2 CC3 UBA
N-ter
C-ter
K549R
ΔCC3
SKITCH LIR CC1 CC2 UBA
N-ter
C-ter
B
Ø Ø WT K549R ΔCC3
6HIS-TAX
Flag-Parkin [h CCCP]
Flag-Parkin
Parkin
FL-TAX
ΔCC3 -TAX
Ubn-TAX
FL-TAX
ΔCC3 -TAX
longer
MFN1
VDAC
TOM20
Ub2-TOM20
Ub1-TOM20
TOM20
longer
COX4
CS
Vinculin
C
Ub-TAX1BP1 signal
2h CCCP
4h CCCP
F
Relative VDAC signal
4h CCCP
G
Relative TOM20 signal
4h CCCP
H
Relative CS signal
4h CCCP
I
Relative COX4 signal
4h CCCP
J
Relative Ub1-TOM20
4h CCCP
D
empty WT KR ΔCC3
HIS-TAX
CCCP
Ub-beads
Phospho-Ubiquitin (Ser65)
Ubiquitin (MAB1050)
Ub-TOM20
TOM20
short
TAX1BP1
long
Pulldown
e WT K Δ
HIS-TAX
CCCP
TAX1BP1
Ubiquitin (MAB1050)
TOM20
TOM20
Vinculin
Input
E
Normalized TAX1BP1 smear (relative to DMSO)
WT
K549R
ΔCC3
4h CCCP

Figure 4

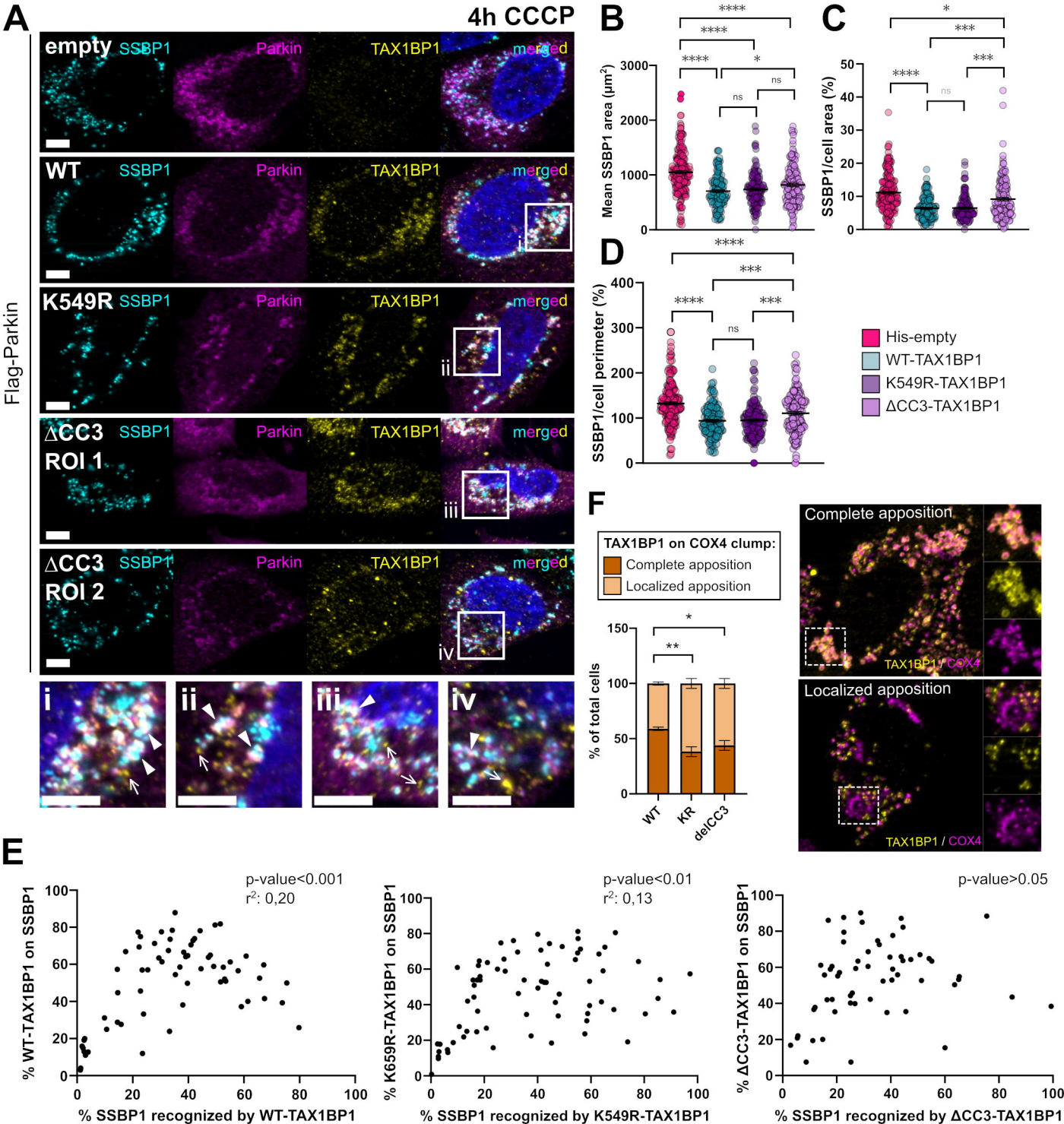
A
4h CCCP
Flag-Parkin
empty
WT
K549R
ΔCC3 ROI 1
ΔCC3 ROI 2
SSBP1
Parkin
TAX1BP1
merged
i
ii
iii
iv
B
Mean SSBP1 area (µm²)
C
SSBP1/cell area (%)
D
SSBP1/cell perimeter (%)
ns
His-empty
WT-TAX1BP1
K549R-TAX1BP1
ΔCC3-TAX1BP1
F
TAX1BP1 on COX4 clump:
Complete apposition
Localized apposition
% of total cells
WT
KR
delCC3
TAX1BP1 / COX4
E
p-value<0.001
r²: 0,20
% WT-TAX1BP1 on SSBP1
% SSBP1 recognized by WT-TAX1BP1
p-value<0.01
r²: 0,13
% K659R-TAX1BP1 on SSBP1
% SSBP1 recognized by K549R-TAX1BP1
p-value>0.05
% ΔCC3-TAX1BP1 on SSBP1
% SSBP1 recognized by ΔCC3-TAX1BP1

Figure 5

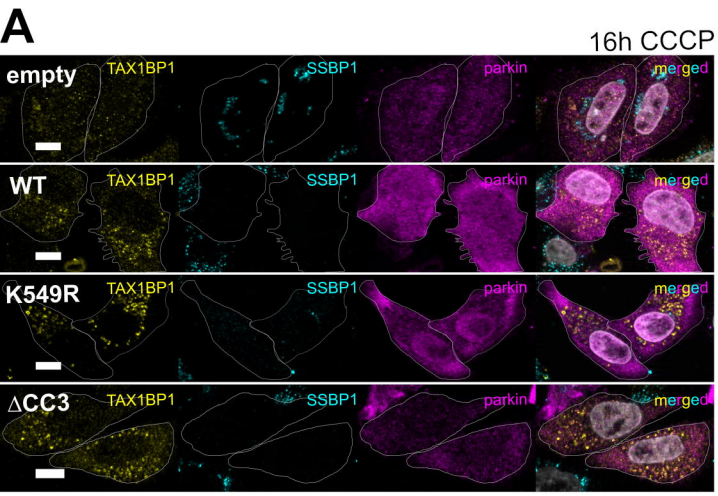
A
16h CCCP
empty
WT
K549R
ΔCC3
TAX1BP1
SSBP1
parkin
merged

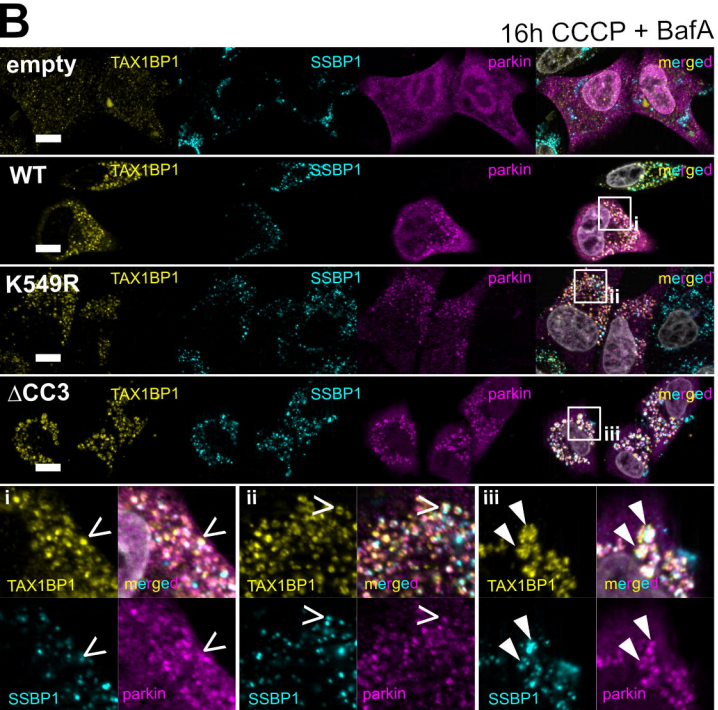
B
16h CCCP + BafA
empty
WT
K549R
ΔCC3
TAX1BP1
SSBP1
parkin
merged
i
ii
iii

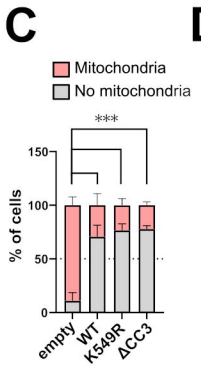
C
Mitochondria
No mitochondria
***
% of cells
150
100
50
0
empty
WT
K549R
ΔCC3

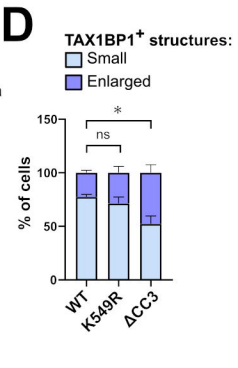
D
TAX1BP1+ structures:
Small
Enlarged
*
ns
% of cells
150
100
50
0
WT
K549R
ΔCC3

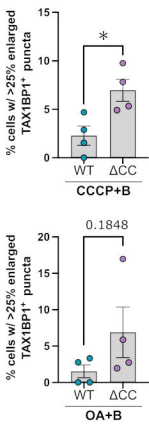
H
% cells w/ >25% enlarged TAX1BP1+ puncta
*
WT
ΔCC
CCCP+B
0.1848
OA+B

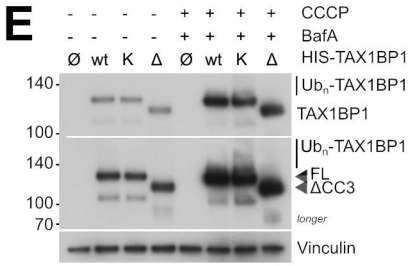
E
CCCP
BafA
HIS-TAX1BP1
Ø wt K Δ Ø wt K Δ
Ubn-TAX1BP1
TAX1BP1
FL
ΔCC3
longer
Vinculin
140
100
70

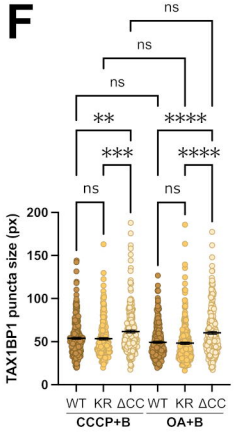
F
TAX1BP1 puncta size (px)
ns
**
***
****
WT KR ΔCC WT KR ΔCC
CCCP+B
OA+B

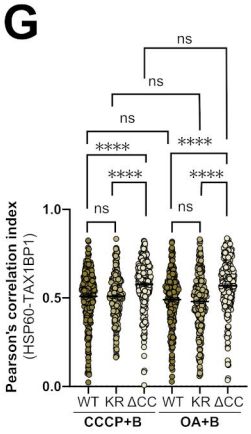
G
Pearson's correlation index (HSP60-TAX1BP1)
ns
****
1.0
0.5
0.0
WT KR ΔCC WT KR ΔCC
CCCP+B
OA+B

Figure 6

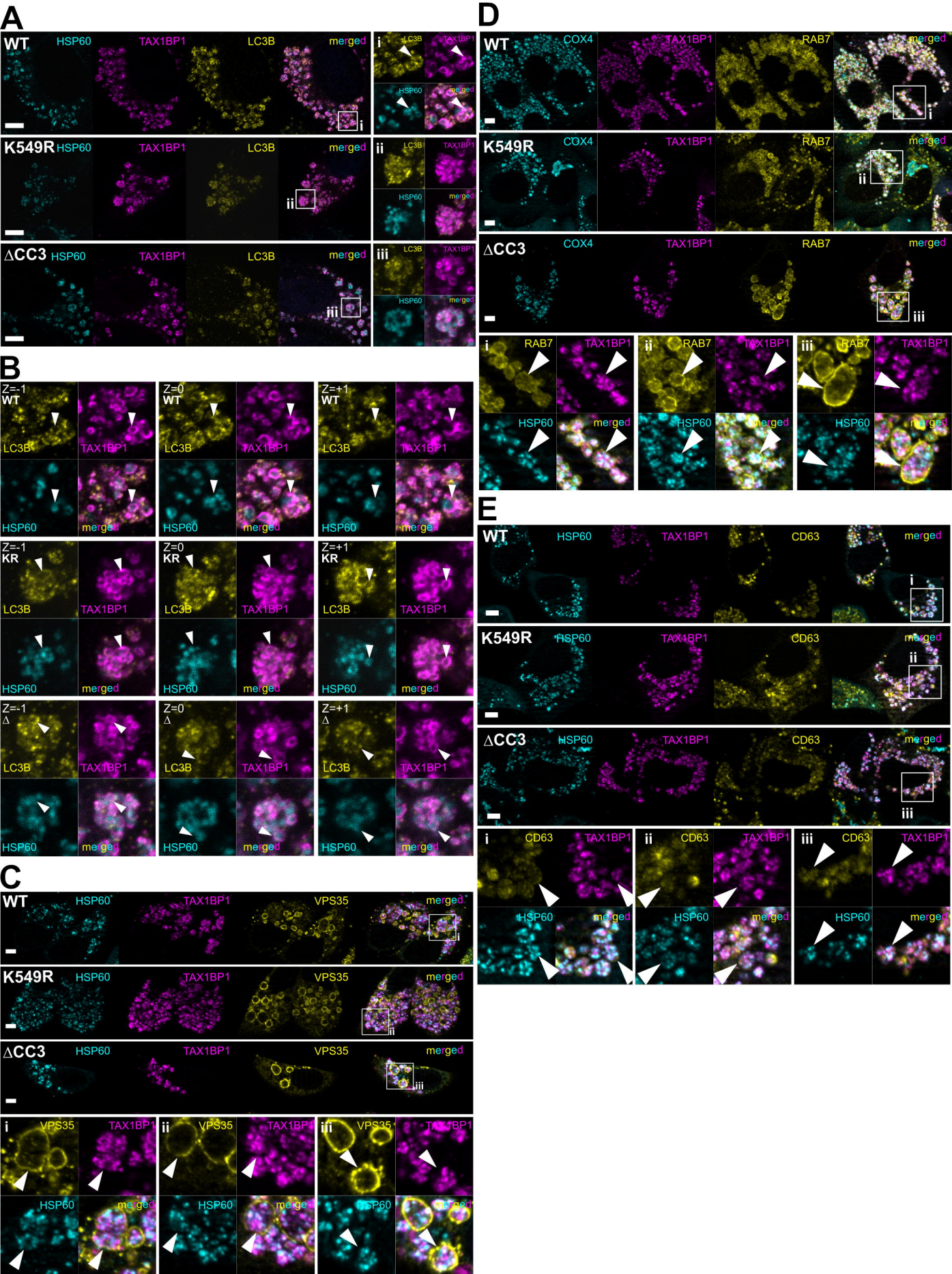
A
WT
HSP60
TAX1BP1
LC3B
merged
i
K549R
ii
ΔCC3
iii
B
Z=-1
Z=0
Z=+1
KR
Δ
C
VPS35
D
COX4
RAB7
E
CD63

Figure 7

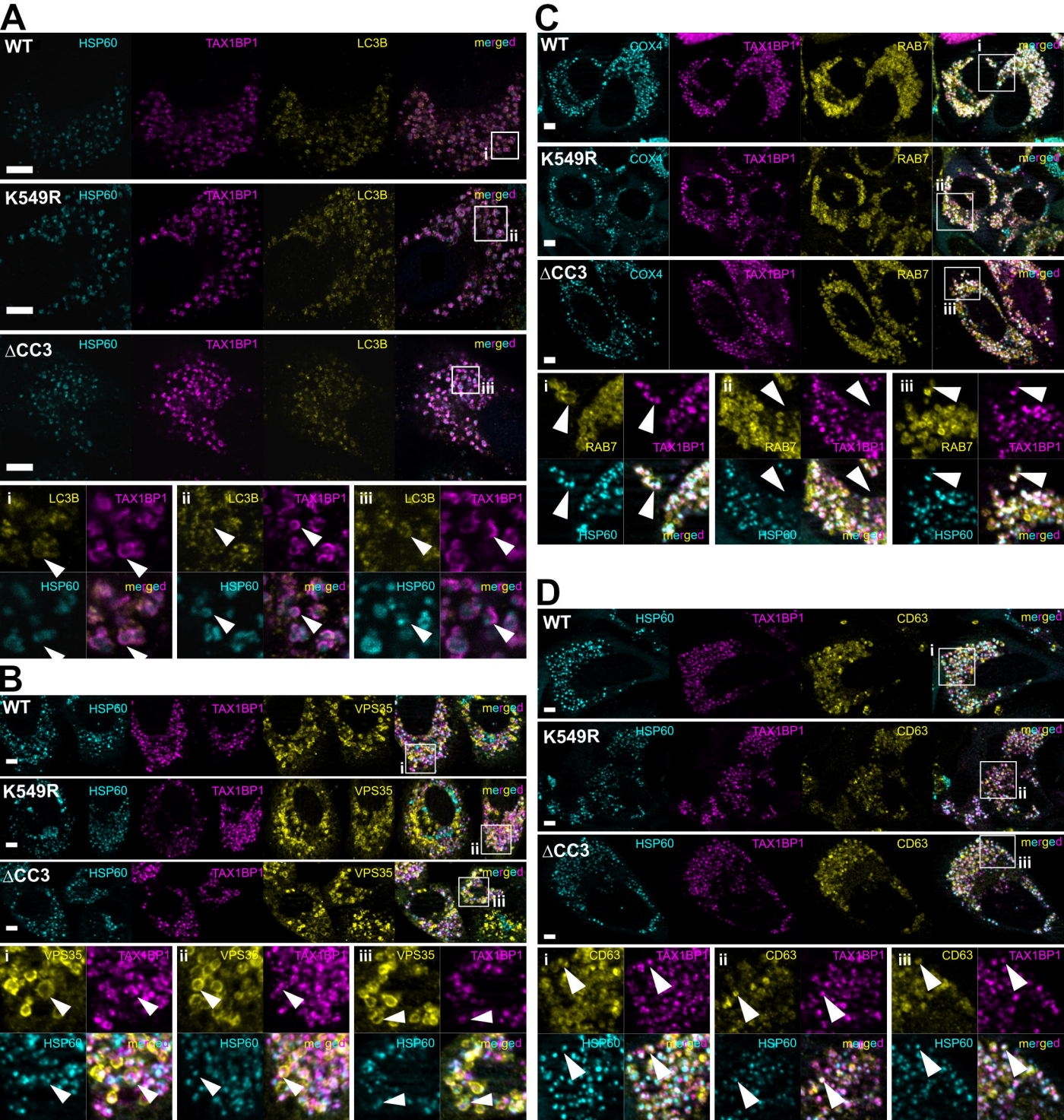
A
WT
HSP60
TAX1BP1
LC3B
merged
i
K549R
HSP60
TAX1BP1
LC3B
merged
ii
ΔCC3
HSP60
TAX1BP1
LC3B
merged
iii
i
LC3B
TAX1BP1
HSP60
merged
ii
LC3B
TAX1BP1
HSP60
merged
iii
LC3B
TAX1BP1
HSP60
merged
B
WT
HSP60
TAX1BP1
VPS35
merged
i
K549R
HSP60
TAX1BP1
VPS35
merged
ii
ΔCC3
HSP60
TAX1BP1
VPS35
merged
iii
i
VPS35
TAX1BP1
HSP60
merged
ii
VPS35
TAX1BP1
HSP60
merged
iii
VPS35
TAX1BP1
HSP60
merged
C
WT
COX4
TAX1BP1
RAB7
merged
i
K549R
COX4
TAX1BP1
RAB7
merged
ii
ΔCC3
COX4
TAX1BP1
RAB7
merged
iii
i
RAB7
TAX1BP1
HSP60
merged
ii
RAB7
TAX1BP1
HSP60
merged
iii
RAB7
TAX1BP1
HSP60
merged
D
WT
HSP60
TAX1BP1
CD63
merged
i
K549R
HSP60
TAX1BP1
CD63
merged
ii
ΔCC3
HSP60
TAX1BP1
CD63
merged
iii
i
CD63
TAX1BP1
HSP60
merged
ii
CD63
TAX1BP1
HSP60
merged
iii
CD63
TAX1BP1
HSP60
merged

Figure 8

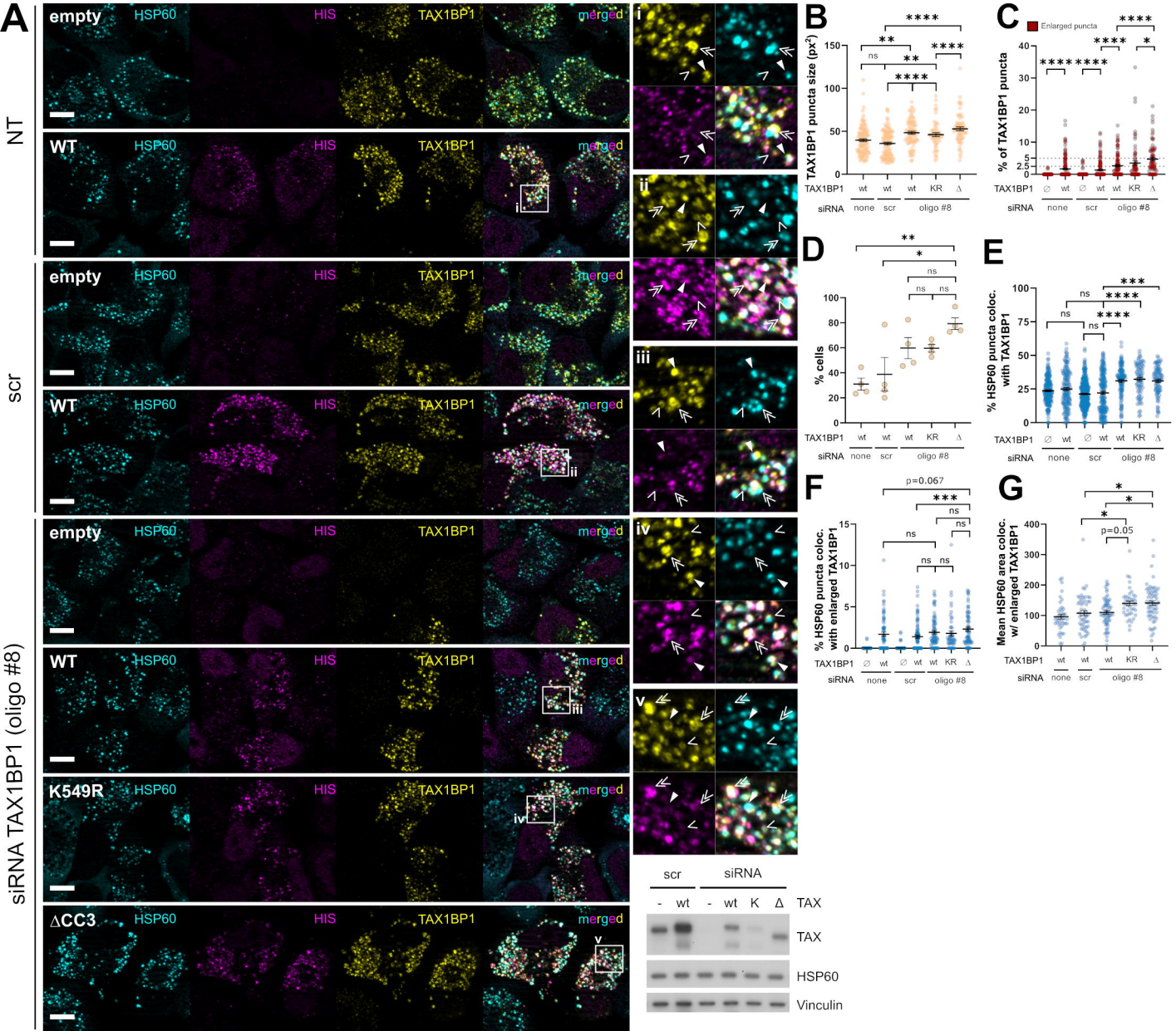
A
NT
scr
siRNA TAX1BP1 (oligo #8)
empty
WT
K549R
ΔCC3
HSP60
HIS
TAX1BP1
merged
i
ii
iii
iv
v
B
TAX1BP1 puncta size (px²)
C
Enlarged puncta
% of TAX1BP1 puncta
D
% cells
E
% HSP60 puncta coloc. with TAX1BP1
F
% HSP60 puncta coloc. with enlarged TAX1BP1
G
Mean HSP60 area coloc. w/ enlarged TAX1BP1
TAX1BP1
siRNA
none
scr
oligo #8
wt
KR
Δ
p=0.067
p=0.05
scr
siRNA
TAX
HSP60
Vinculin

Figure 9

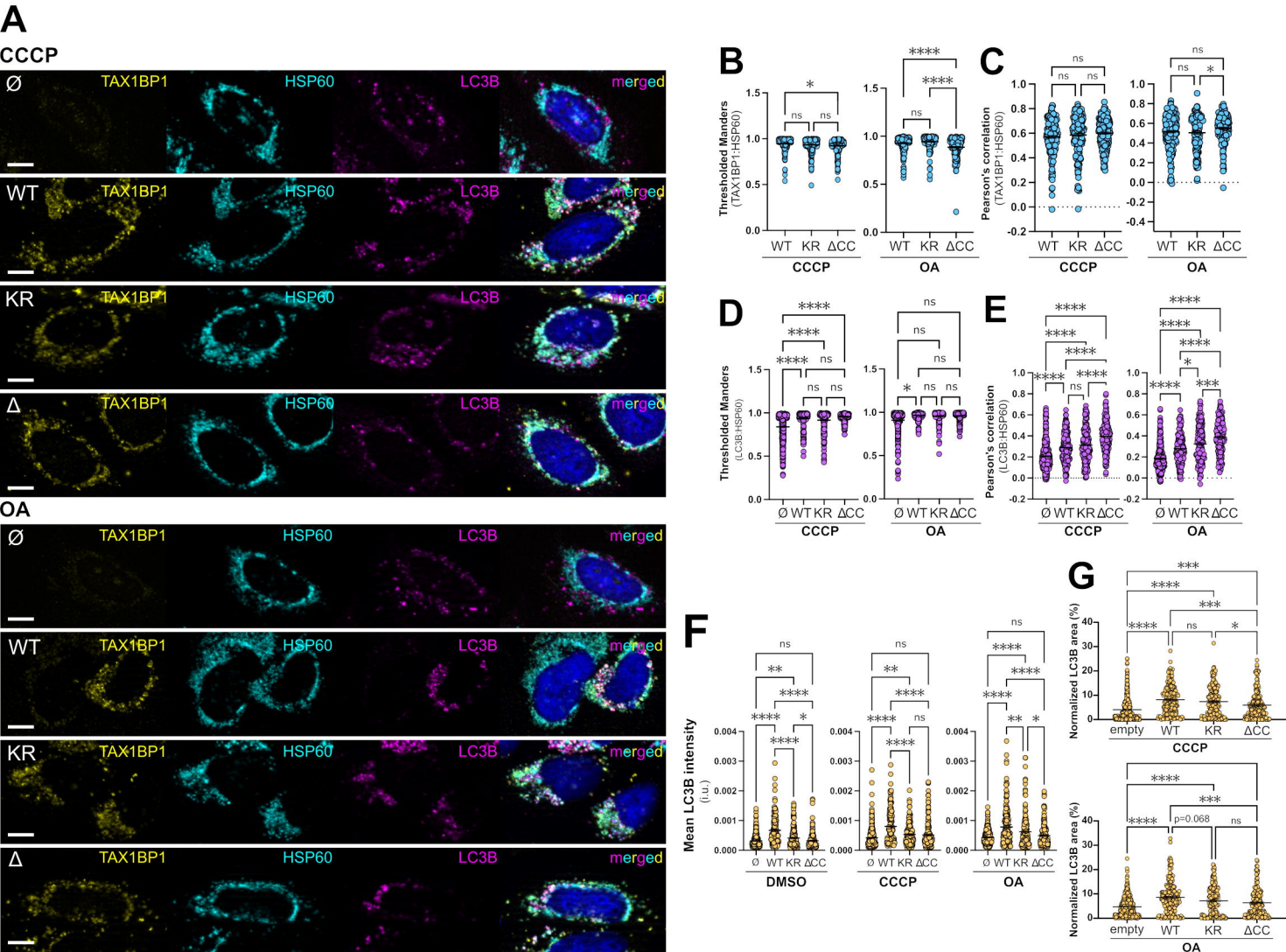
A
CCCP
Ø
WT
KR
Δ
OA
TAX1BP1
HSP60
LC3B
merged
B
Thresholded Manders (TAX1BP1:HSP60)
WT KR ΔCC
CCCP
OA
C
Pearson's correlation (TAX1BP1:HSP60)
D
Thresholded Manders (LC3B:HSP60)
E
Pearson's correlation (LC3B:HSP60)
F
Mean LC3B intensity (i.u.)
DMSO
G
Normalized LC3B area (%)
empty
p=0.068

Figure 10

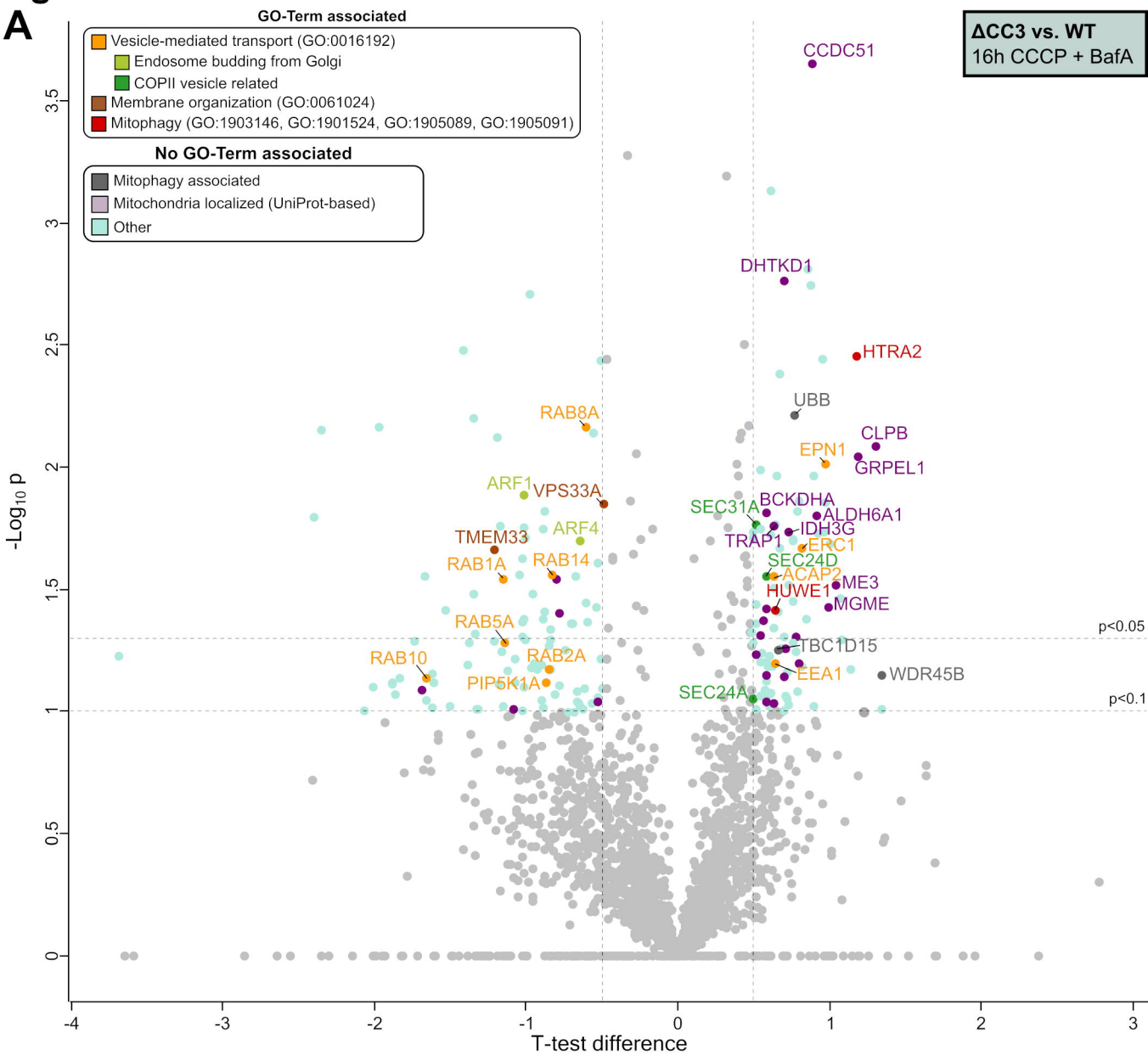
A
GO-Term associated
Vesicle-mediated transport (GO:0016192)
Endosome budding from Golgi
COPII vesicle related
Membrane organization (GO:0061024)
Mitophagy (GO:1903146, GO:1901524, GO:1905089, GO:1905091)
No GO-Term associated
Mitophagy associated
Mitochondria localized (UniProt-based)
Other
ΔCC3 vs. WT
16h CCCP + BafA
CCDC51
DHTKD1
HTRA2
UBB
CLPB
EPN1
GRPEL1
RAB8A
ARF1
VPS33A
SEC31A
BCKDHA
ALDH6A1
IDH3G
TRAP1
ERC1
SEC24D
ACAP2
ME3
HUWE1
MGME
TMEM33
ARF4
RAB1A
RAB14
RAB5A
RAB10
RAB2A
PIP5K1A
TBC1D15
EEA1
WDR45B
SEC24A
p<0.05
p<0.1
-Log10 p
T-test difference

B
ΔCC3 vs. WT
down
up
organic acid metabolic process
DNA metabolic process
DNA repair
dsDNA break repair via break−induced replication
DNA replication
regulation of DNA replication
DNA conformation change
mRNA 3'−splice site recognition
U2−type prespliceosome assembly
response to mitochondrial depolarization
positive regulation of mitophagy
protein transport
vesicle−mediated transport
nuclear transport
nucleocytoplasmic transport
membrane organization
vesicle organization
vesicle localization
vesicle budding from membrane
membrane fusion
Golgi vesicle transport
ER to Golgi vesicle−mediated transport
positive regulation of telomerase RNA loc. to Cajal body
mitochondrial ADP transmembrane transport
−LOG10 P−value
LOG2 fold enrichment

Figure 11

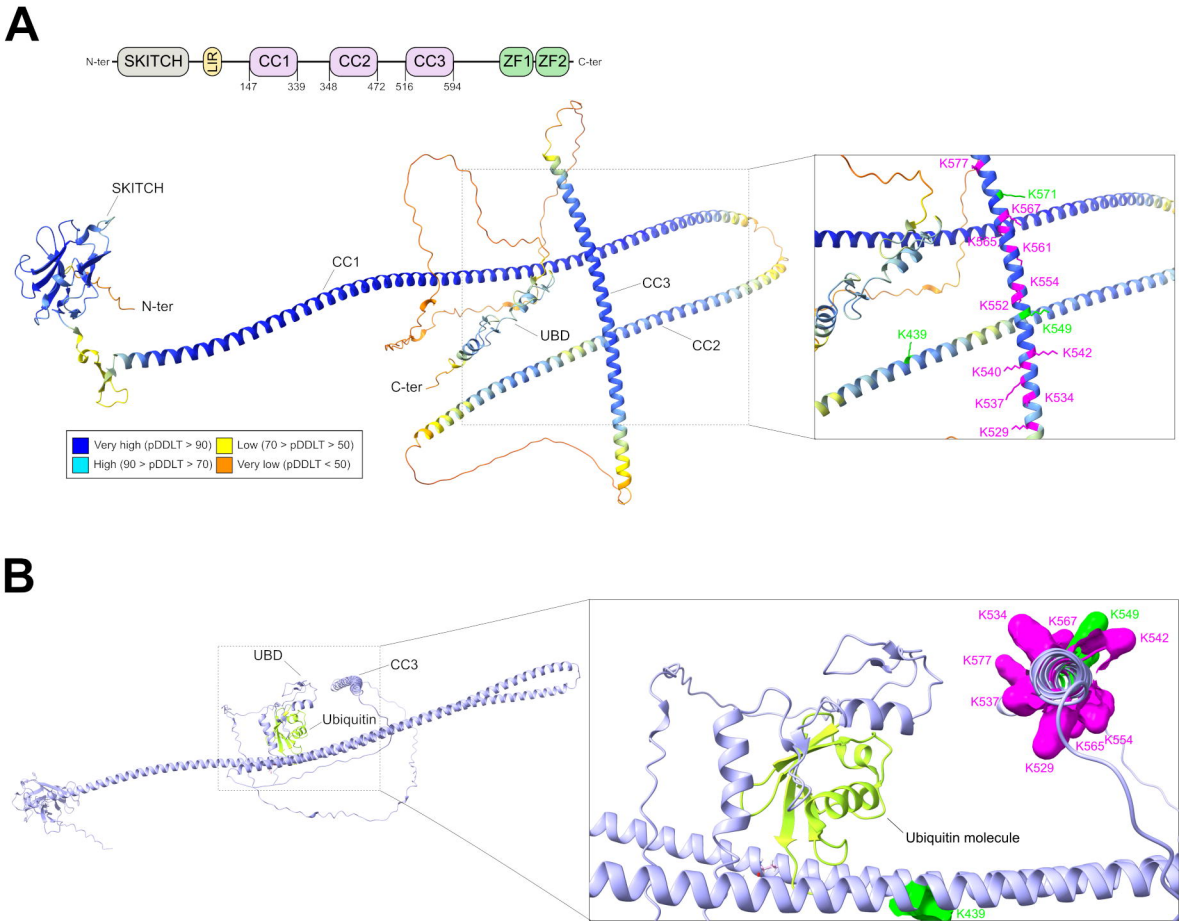
A
N-ter
SKITCH
LIR
CC1
CC2
CC3
ZF1
ZF2
C-ter
147
339
348
472
516
594
SKITCH
N-ter
CC1
CC3
UBD
CC2
C-ter
K577
K571
K567
K565
K561
K554
K552
K549
K542
K439
K540
K537
K534
K529
Very high (pDDLT > 90)
Low (70 > pDDLT > 50)
High (90 > pDDLT > 70)
Very low (pDDLT < 50)
B
UBD
CC3
Ubiquitin
K63
K48
K534
K567
K549
K542
K577
K537
K565
K554
K529
Ubiquitin molecule
K439

Figure 12

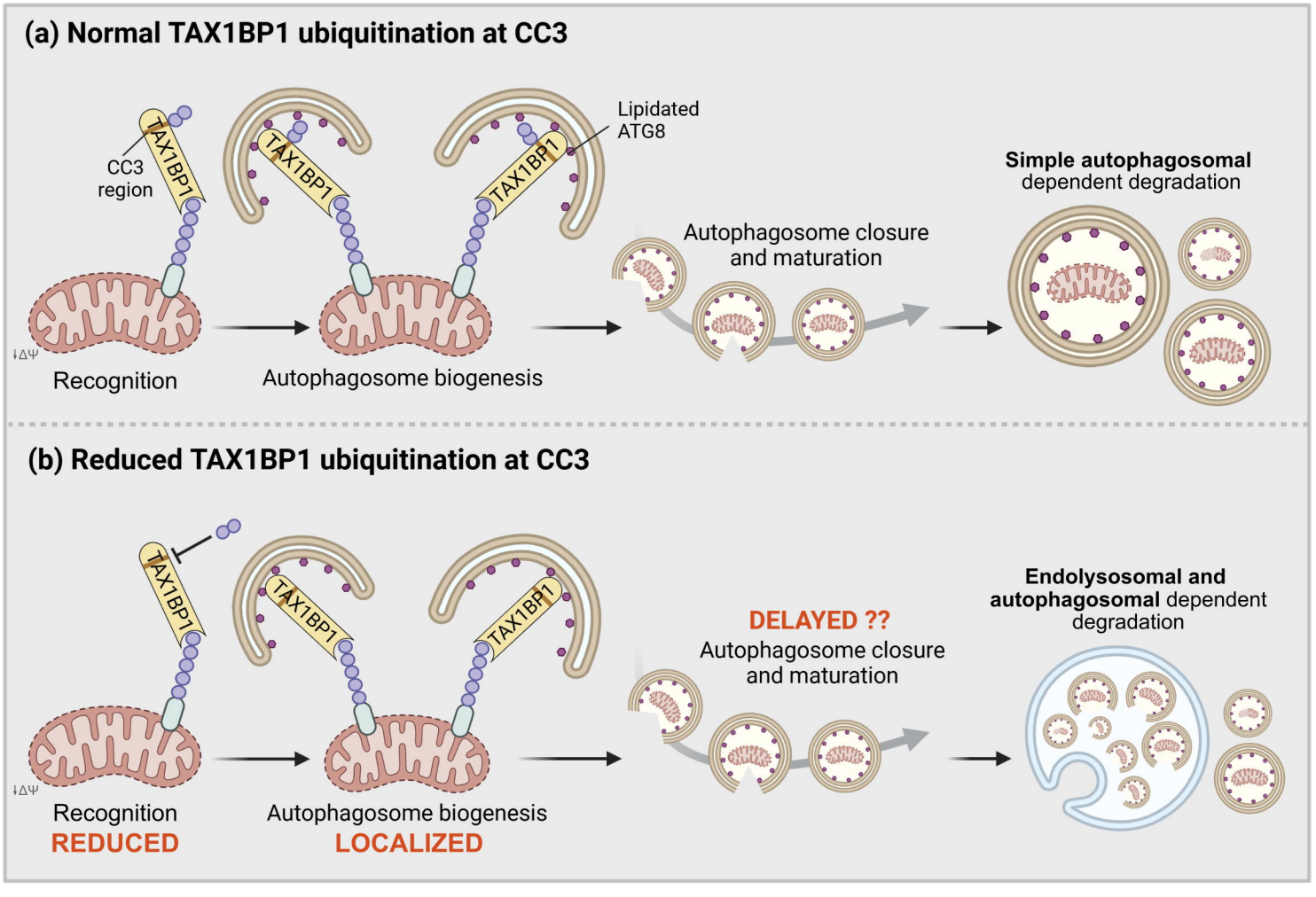
(a) Normal TAX1BP1 ubiquitination at CC3
CC3 region
TAX1BP1
TAX1BP1
TAX1BP1
Lipidated ATG8
Recognition
Autophagosome biogenesis
Autophagosome closure and maturation
Simple autophagosomal dependent degradation
(b) Reduced TAX1BP1 ubiquitination at CC3
TAX1BP1
TAX1BP1
TAX1BP1
Recognition
REDUCED
Autophagosome biogenesis
LOCALIZED
DELAYED ??
Autophagosome closure and maturation
Endolysosomal and autophagosomal dependent degradation